

Can High-velocity Protostellar Jets Help to Drive Low-velocity Outflow?

Masahiro N. Machida¹

¹ *Department of Earth and Planetary Sciences, Faculty of Sciences, Kyushu University, Fukuoka, Fukuoka 819-0395, Japan*

Accepted XXX. Received YYY; in original form ZZZ

ABSTRACT

Using three-dimensional magnetohydrodynamics simulations, the driving of protostellar jets is investigated in different star-forming cores with the parameters of magnetic field strength and mass accretion rate. Powerful high-velocity jets appear in strongly magnetized clouds when the mass accretion rate onto the protostellar system is lower than $\dot{M} \lesssim 10^{-3} M_{\odot} \text{ yr}^{-1}$. On the other hand, even at this mass accretion rate range, no jets appear for magnetic fields of prestellar clouds as weak as $\mu_0 \gtrsim 5\text{--}10$, where μ_0 is the mass-to-flux ratio normalized by the critical value $(2\pi G^{1/2})^{-1}$. For $\dot{M} \gtrsim 10^{-3} M_{\odot} \text{ yr}^{-1}$, although jets usually appear just after protostar formation independent of the magnetic field strength, they soon weaken and finally disappear. Thus, they cannot help drive the low-velocity outflow when there is no low-velocity flow just before protostar formation. As a result, no significant mass ejection occurs during the early mass accretion phase either when the prestellar cloud is weakly magnetized or when the mass accretion rate is very high. Thus, protostars formed in such environments would trace different evolutionary paths from the normal star formation process.

Key words: MHD – stars: formation – stars: protostars – stars: magnetic field – stars: winds, outflows – protoplanetary disks

1 INTRODUCTION

Protostellar outflows (low-velocity wide-angle outflows and high-velocity collimated jets) are ubiquitously observed in various star-forming regions (Wu et al. 2004). They are considered to universally appear in the star formation process. Outflows are powered by accreting matter, in which the gravitational energy of the accreting matter is converted into the outflow kinetic energy through the magnetic field (or via magnetic energy; Uchida & Shibata 1985; Blandford & Payne 1982; Tomisaka 2002). Past studies have shown that protostellar outflow

is necessary for removing the angular momentum of star-forming clouds (Tomisaka 2000; Joos, Hennebelle, & Ciardi 2012; Masson et al. 2016; Hirano et al. 2020). In addition, the star formation efficiency should be related to the mass ejection rate of the outflow, as a large fraction of the cloud mass is ejected by the protostellar outflow (Matzner & McKee 2000; Arce et al. 2007; Machida & Hosokawa 2013). Thus, the protostellar outflow plays significant roles in the star formation process (Tanaka et al. 2017, 2018). Nevertheless, some objects (or protostars) have been observed to show no sign of outflow (e.g. Tokuda et al. 2018; Aso et al. 2019).

In previous studies (Matsushita et al. 2017, 2018; Machida & Hosokawa 2020, hereafter Papers I, II and III), we investigated the driving condition of low-velocity outflows in various star-forming cloud cores. After performing long-term simulations, we concluded that low-velocity outflow fails to appear or is delayed when the magnetic field of the star-forming core is weak and/or when the mass accretion rate onto the central region is high (see also Wurster, Price, & Bate 2016 and Lewis & Bate 2017). We called these cases “failed or delayed outflows” and showed that they correspond to the objects that were observed to show no protostellar outflow (Aso et al. 2019). For the failed and delayed outflow cases, a high ram pressure of the infalling envelope suppresses the outflow driving (see, Papers I and III). In addition, for the delayed outflow case, the outflow begins to evolve only after a large part of the infalling envelope dissipates, because the ram pressure of the envelope weakens as the density of the infalling envelope becomes low (Paper III). However, there has been criticism about the numerical settings regarding the failed and delayed outflow cases. In our previous studies (Papers I–III), we did not resolve the protostar itself. Instead of resolving the protostar, we used sink cells which cover both the inner disk region and protostar. Although the sink cell method can accelerate the time evolution of star-forming clouds in the simulation, the region around the protostar cannot be resolved (Machida et al. 2010). Thus, we could not simulate a high-velocity outflow component (i.e. high-velocity jet) driven near the protostar. Note that high-velocity components can be seen in the high-spatial resolution simulations of low-mass star formation (Tomisaka 2002; Banerjee & Pudritz 2006; Machida, Inutsuka, & Matsumoto 2006; Tomida et al. 2013; Bate, Tricco, & Price 2014; Machida 2014; Lewis & Bate 2017; Vaytet et al. 2018; Machida & Basu 2019). Note also that few studies focused on the outflow in the high-mass star formation simulations with sink cells, in which the flows driven near the protostar were not spatially resolved (Seifried et al. 2011, 2012; Kölligan & Kuiper 2018).

In both observational and theoretical works, it is well known that two types of flow appear in the star formation process (e.g. [Arce et al. 2007](#); [Machida, Inutsuka, & Matsumoto 2008](#)). A high-velocity collimated flow (so-called high-velocity jets) appears near the protostar, while a low-velocity wide-angle flow (so-called low-velocity outflow) appears in the region far from the protostar or in the outer edge of the disk (see review by [Inutsuka 2012](#)). Note that no flow appears in the intermediate disk region because the magnetic field is not well coupled with neutrals ([Machida, Inutsuka, & Matsumoto 2007](#); [Xu & Kunz 2021](#)). In our previous studies (Papers I–III), we did not resolve the high-velocity jets. Thus, if the protostar and the disk inner region are spatially resolved, high-velocity jets possibly appear and may help to drive a wide-angle flow (or low-velocity outflow). In other words, even if the low-velocity outflow does not appear in a simulation using sink cells, it may appear with help from high-velocity jets in high-resolution simulations without sink cells. In addition, there is a long-standing debate about driving wide-angle low-velocity outflows. There are two conflicting models or scenarios for driving low-velocity outflow, the entrainment and direct-driven scenarios. The low-velocity outflow is entrained by the high-velocity jets in the former model ([Arce et al. 2007](#)), while the low-velocity outflow is driven directly from the outer disk region in the latter ([Matsushita et al. 2019](#)). Although both recent observations and numerical simulations support the direct driven scenario ([Hennebelle & Fromang 2008](#); [Machida 2014](#); [Bjerkeli et al. 2016](#); [Hirota et al. 2017](#); [Alves et al. 2017](#); [Tabone et al. 2018](#); [de Valon et al. 2020](#); [Lee et al. 2021](#); [Marchand et al. 2020](#); [Wurster, Bate, & Bonnell 2021](#)), entrainment may not be completely rejected. It may be possible for the high-velocity jets to entrain a part of the infalling gas and produce the low-velocity component.

In Paper III using simulations with sink cells, I showed that the low-velocity outflow fails to appear or appears in a late stage in weakly magnetized clouds when the mass accretion rate onto the central region is high. In this study, I investigate whether the high-velocity flow can appear and contribute to driving the low-velocity outflow with almost the same settings as in Paper III but without using sink cells, in which the protostar is spatially resolved with a spatial resolution of 7.9×10^{-3} au.

The structure of this paper is as follows. The numerical settings and methods are described in §2 and the calculation results are presented in §3. I discuss the effect of the high-velocity jets on the low-velocity outflow in §4. A summary is presented in §5.

Model	f	μ_0	B_0 [G]	Ω_0 [s^{-1}]	α_0	β_0	γ_0	M_{cl} [M_\odot]	Jet	Outflow
AM3	1.4	3	1.0×10^{-5}	3.2×10^{-14}	0.5	0.02	0.083	11	S	S
AM5	1.4	5	6.2×10^{-6}	3.2×10^{-14}	0.5	0.02	0.030	11	N	D
AM10	1.4	10	3.1×10^{-6}	3.2×10^{-14}	0.5	0.02	7.5×10^{-3}	11	N	D
AM20	1.4	20	1.6×10^{-6}	3.2×10^{-14}	0.5	0.02	1.9×10^{-3}	11	N	D
BM3	3.4	3	2.5×10^{-5}	5.0×10^{-14}	0.2	0.02	0.083	28	S	S
BM5	3.4	5	1.5×10^{-5}	5.0×10^{-14}	0.2	0.02	0.030	28	N	D
BM10	3.4	10	7.5×10^{-6}	5.0×10^{-14}	0.2	0.02	7.5×10^{-3}	28	N	F
BM20	3.4	20	3.7×10^{-6}	5.0×10^{-14}	0.2	0.02	1.9×10^{-3}	28	N	F
CM3	8.4	3	6.2×10^{-5}	7.9×10^{-14}	0.08	0.02	0.083	68	S	S
CM5	8.4	5	3.7×10^{-5}	7.9×10^{-14}	0.08	0.02	0.030	68	W	F
CM10	8.4	10	1.9×10^{-5}	7.9×10^{-14}	0.08	0.02	7.5×10^{-3}	68	W	F
CM20	8.4	20	6.2×10^{-6}	7.9×10^{-14}	0.08	0.02	1.9×10^{-3}	68	W	F
DM3	16.8	3	1.2×10^{-4}	1.1×10^{-13}	0.04	0.02	0.083	132	S	S
DM5	16.8	5	7.4×10^{-5}	1.1×10^{-13}	0.04	0.02	0.030	132	W	F
DM10	16.8	10	3.7×10^{-5}	1.1×10^{-13}	0.04	0.02	7.5×10^{-3}	132	W	F
DM20	16.8	20	1.8×10^{-5}	1.1×10^{-13}	0.04	0.02	1.9×10^{-3}	132	W	F
EM3	33.6	3	2.4×10^{-4}	1.5×10^{-13}	0.02	0.02	0.030	272	N	S
EM5	33.6	5	1.5×10^{-4}	1.5×10^{-13}	0.02	0.02	0.083	272	W	D
EM10	33.6	10	7.4×10^{-5}	1.5×10^{-13}	0.02	0.02	7.5×10^{-3}	272	N	F
FM3	67.2	3	5.0×10^{-4}	2.2×10^{-13}	0.01	0.02	0.083	545	N	D
FM5	67.2	5	3.0×10^{-4}	2.2×10^{-13}	0.01	0.02	0.030	545	N	D
FM10	67.2	10	1.5×10^{-5}	2.2×10^{-13}	0.01	0.02	7.5×10^{-3}	545	W	D

Table 1. Model name, initial cloud parameters and calculation results. Column 1 gives the model name. Columns 2 and 3 give the parameters f and μ_0 . Columns 4 and 5 give the magnetic field strength B_0 and angular velocity Ω_0 for the initial state. Columns 6–8 give the ratios of the thermal α_0 , rotational β_0 and magnetic γ_0 energies to the gravitational energy of the initial cloud. Column 9 gives the initial cloud mass. Column 10 describes the calculation results of this study, in which ‘S’, ‘W’ and ‘N’ means that a strong, weak and no jet appears, respectively. Column 11 describes the calculation results of Paper III, in which ‘S’, ‘D’ and ‘F’ mean that an outflow successfully appears, a delayed outflow appears and no (or failed) outflow appears, respectively.

2 INITIAL CONDITIONS AND NUMERICAL SETTINGS

The initial conditions and numerical settings are almost the same as in Papers I–III. Thus, I only briefly explain them in this section. As the initial state, I adopt a spherical cloud core with a Bonnor–Ebert (B.E.) density profile with a central density of $n_{c,0} = 10^5 \text{ cm}^{-3}$ and an isothermal temperature of $T_{\text{iso},0} = 20 \text{ K}$. The initial cloud has twice the critical B.E. radius ($R_{\text{cl}} = 4.1 \times 10^4 \text{ au}$). The cloud density is enhanced by a factor of f to promote gravitational collapse, in which f is the density enhancement factor (Papers I and III) and is related to the cloud (thermal) stability α_0 (ratio of thermal to gravitational energy). Therefore, the initial cloud has a central density of $n_{\text{cl}} = f \times 10^5 \text{ cm}^{-3}$ ($= f \times n_{c,0}$). A uniform density $n_{\text{ISM}} = 1.25 \times 10^{-2} n_{\text{cl}}$ is set outside the initial cloud ($r > R_{\text{cl}}$).

A uniform magnetic field B_0 is imposed over the whole computational domain. The magnetic field direction is set to be parallel to the z -axis. A rigid rotation Ω_0 is adopted within

the cloud ($r < R_{\text{cl}}$) and the rotation axis is set to be inclined by θ_0 toward the x -axis from the z -axis. Thus, the initial magnetic field is misaligned with the initial rotation axis. On the other hand, an initial magnetic field parallel to the initial rotation axis was adopted in Papers I–III. Recently, we have shown that the aligned cases are not very realistic (Hirano & Machida 2019; Hirano et al. 2020; Machida, Hirano, & Kitta 2020), because the disk normal, the propagation direction of the outflow and jets and the angular momentum vector of the disk and protostar are well aligned, and the angular momentum in such systems is transported only in specific directions (for details, see Ciardi & Hennebelle 2010; Joos, Hennebelle, & Ciardi 2012; Hirano et al. 2020). Thus, the misaligned case should be adopted as a general (or realistic) case. In this study, to limit the number of models, referring to the results in Machida, Hirano, & Kitta (2020), I fixed the angle θ_0 to be $\theta_0 = 20^\circ$, which can yield strong outflow and jets in the low-mass star-formation process (Lewis, Bate, & Price 2015; Machida, Hirano, & Kitta 2020).

As the initial state, a total of 22 different prestellar clouds are prepared (Table 1), in which the density enhancement factor f (or α_0) and the normalized mass-to-flux ratio μ_0 (or magnetic field strength B_0) are parameters. The parameter α_0 (or f) controls the mass accretion rate onto the central region \dot{M} , in which the mass accretion rate is proportional to $\alpha_0^{-3/2}$ (for details, see Paper I). I will detail the mass accretion rate for some of the models in §3.1. In this series of studies, the mass accretion rate parameter (or α_0) determines whether star in formation is low- or high-mass. The normalized mass-to-flux ratio is defined as

$$\mu_0 \equiv \left(\frac{M_{\text{cl}}}{\Phi_{\text{cl}}} \right) / \left(\frac{1}{2\pi G^{1/2}} \right), \quad (1)$$

where Φ_{cl} is the magnetic flux of the initial cloud. The initial magnetic field strength B_0 is adjusted so that the mass-to-flux ratio becomes $\mu_0 = 3, 5, 10$ and 20 in each initial cloud. The rotation rate Ω_0 is determined to give $\beta_0 = 0.02$ in each model, where β_0 is the ratio of the rotational to gravitational energy. The model name and cloud parameters are described in Table 1¹. Except for the angle θ_0 between the initial magnetic field direction and the rotation axis, the initial clouds are completely the same as in Paper III.

The numerical settings are almost the same as in Papers I–III. The basic equations (resistive MHD equations) are described in equations (1)–(4) of Machida & Basu (2019) and equation (1) of Machida (2014). The nested grid code is used to cover both prestellar core

¹ I do not include models EM20 and FM20 to further limit the number of models. Since these models have a high mass accretion rate and high infall velocity, a very long calculation time is necessary to complete the calculation.

and protostar (for details of the code, see [Machida et al. 2004](#); [Machida et al. 2005a](#); [Machida et al. 2010](#); [Machida & Hosokawa 2013](#)). At the beginning of the calculation, five levels, l , of nested grids are prepared. Each grid is composed of $(i, j, k) = (64, 64, 64)$. The initial prestellar cloud is set in the fifth level of the grid ($l = 5$). The first level of the grid has a box size of $L(l = 1) = 6.6 \times 10^5$ au and a cell width of $h(l = 1) = 1.0 \times 10^4$ au. Both the box size and cell width halve with each increment of grid level l . A new finer grid is generated to satisfy the Truelove condition, in which the Jeans length is resolved with at least 16 cells ([Truelove et al. 1997](#)). The maximum grid level is set to $l_{\max} = 21$, which has a box size of $L(l = l_{\max}) = 0.51$ au and a cell width of $h(l = l_{\max}) = 7.9 \times 10^{-3}$ au.

For the purpose of reference, I describe the difference in the numerical settings between this study and Papers I–III. In Papers I–III, the central region is covered by the sink cells with a spatial resolution of $h = 0.62$ au and a sink radius of $r_{\text{sink}} = 1$ au, while in this study the protostar is resolved with $h = 7.9 \times 10^{-3}$ au without using sink cells. The detailed settings can be confirmed in [Machida \(2014\)](#) and [Machida & Nakamura \(2015\)](#). A small time step is required with a high spatial resolution to ensure the Courant, Friedrichs and Lewy condition. Thus, the simulation could be executed for about 10,000 yr after protostar formation in Paper III, while only for ~ 500 yr after protostar formation in this study.

3 RESULTS

The evolution of outflows and jets for the models listed in Table 1 are presented in this section. As described in §2, two parameters, the mass-to-flux ratio μ_0 (corresponding to magnetic field strength) and thermal stability α_0 (corresponding to mass accretion rate), are used to characterize the models. This section first focusses on the evolution of jets for models with strong magnetic fields (AM3, BM3, CM3, DM3, EM3, FM3). Then, the jet driving for all the models in Table 1 is shown.

In this paper, as shown in previous studies ([Tomisaka 2002](#); [Banerjee & Pudritz 2006](#); [Machida 2014](#); [Machida & Basu 2019](#)), two components, the low-velocity outflow and high-velocity jet, appear from different disk regions. However, it is very difficult to distinguish them. Thus, I simply call all the outflowing gas components including the low-velocity outflow and high-velocity jet the ‘outflow’ in this section. In addition, I describe the high-velocity outflow component as ‘the high-velocity jet (or high-velocity component)’, and the low-velocity outflow as ‘the low-velocity outflow (or low-velocity component)’, though there

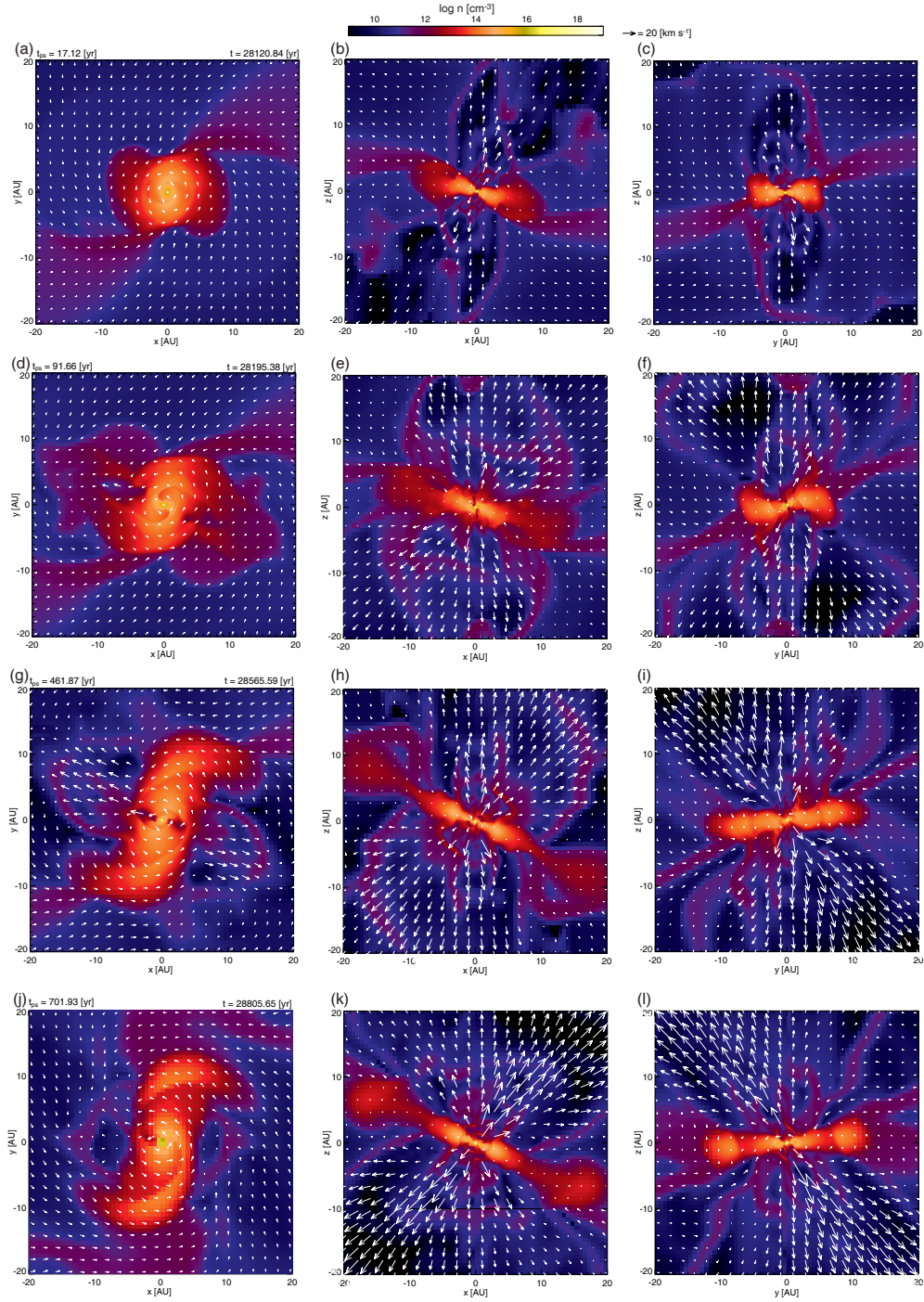


Figure 1. Density (color) and velocity (arrows) distributions at different epochs on the $z = 0$ (left panels), $y = 0$ (middle panels) and $x = 0$ (right panels) planes for DM3 (see also DM3.avi). The elapsed time t_{ps} after protostar formation and that t after the beginning of the cloud collapse are described in each left panel.

is no clear velocity boundary between them. It should be noted that, in Papers I–III, since the high-velocity component was not resolved and does not appear, the low-velocity flow (i.e. all the outflowing gas) was referred to as the outflow.

3.1 Outflow Evolution for Strongly Magnetic Field Models

Firstly, the cloud evolutions for DM3, EM3 and FM3 are shown. Figure 1 shows the time sequence of the central region around the protostar for DM3 with the density and velocity distributions on the $z = 0$ (left), $y = 0$ (middle) and $x = 0$ (right) planes plotted. DM3 has the parameters $\mu_0 = 3$ and $\alpha_0 = 0.04$. We can confirm a rotationally supported disk with a size of ~ 10 au at the very early accretion phase (Fig. 1a). At the same epoch, the outflow extends to ~ 20 au (Figs. 1b and c). The size growth of the rotationally supported disk can be confirmed in the density distribution on the $y = 0$ plane (nearly edge-on view) in Figures 1b, e, h and k, in which the disk-like structure gradually increases in size. Although the direction of the disk normal changes over time (Hirano & Machida 2019), the rotation motion in the disk is roughly confirmed on the $z = 0$ plane (Figs. 1a, d, g, j).

Figure 1 also shows that strong mass ejection frequently occurs as the disk grows. Shell-like structures seen in Figures 1f, h and i are caused by episodic mass ejection (Hirano & Machida 2019), in which each shell roughly corresponds to each episode of mass ejection. Although the direction of the outflow changes with time, the strong mass ejection lasts until the end of the simulation, as also seen in Machida, Hirano, & Kitta (2020). The maximum speed of the outflowing gas exceeds ~ 100 km s $^{-1}$. Violent mass ejection by the high-velocity jet can be seen in Figure 1h, i, k and l.

Figure 2 shows the time sequence of the region around the protostar for EM3 with parameters $\mu_0 = 3$ and $\alpha_0 = 0.02$. For this model, the low-velocity outflow appears before protostar formation and creates a clear cocoon-like structure, as seen in Figure 2c and f. A high-velocity jet begins to appear after protostar formation (Fig. 2b). Then, strong mass ejection occurs around the protostar at $t_{\text{ps}} \sim 100$ yr (Fig. 2e), where t_{ps} is the elapsed time after protostar formation. On the other hand, Figures 2c and f indicate that the low-velocity outflow weakens and the cocoon-like structure gradually shrinks. Figure 2f shows that the high-velocity jet propagates into the shrinking cocoon-like structure formed by the low-velocity outflow. The high-velocity jet also gradually loses activity for $t_{\text{ps}} \gtrsim 150$ yr (Figs. 2h and i). Finally, the strong mass ejection stops and both the low-velocity outflow and high-velocity jet disappear, as seen in Figure 2k and l. The regions above and below the protostar and disk are disturbed by the outflow and have complicated structures just after protostar formation (Figs. 2c and f). On the other hand, the density distribution is rather smooth and

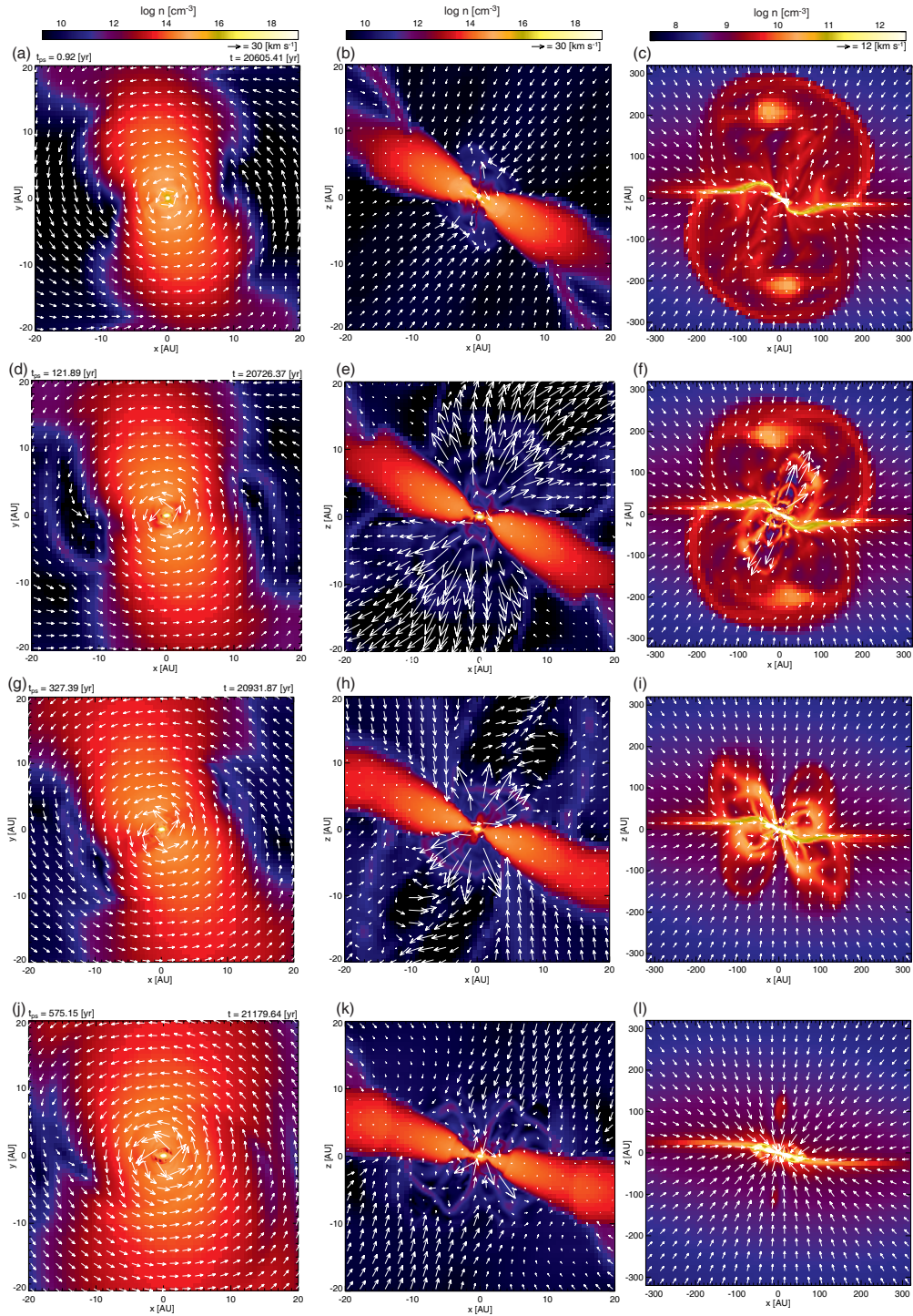


Figure 2. Density (color) and velocity (arrows) distributions at different epochs on the $z = 0$ (left panels) and $y = 0$ (middle and right panels) planes for EM3 (see also EM3.avi). Note that the box scale of the left and middle panels is different from that of the right panels. The elapsed time t_{ps} after protostar formation and that t after the beginning of the cloud collapse are described in each left panel.

no particular structure is seen in these regions at $t_{\text{ps}} \simeq 500$ yr (Fig. 2l). However, a very weak jet appears in the region very close to the protostar (Fig. 2k).

Figure 3 shows the time sequence of the region around the protostar for FM3 which has

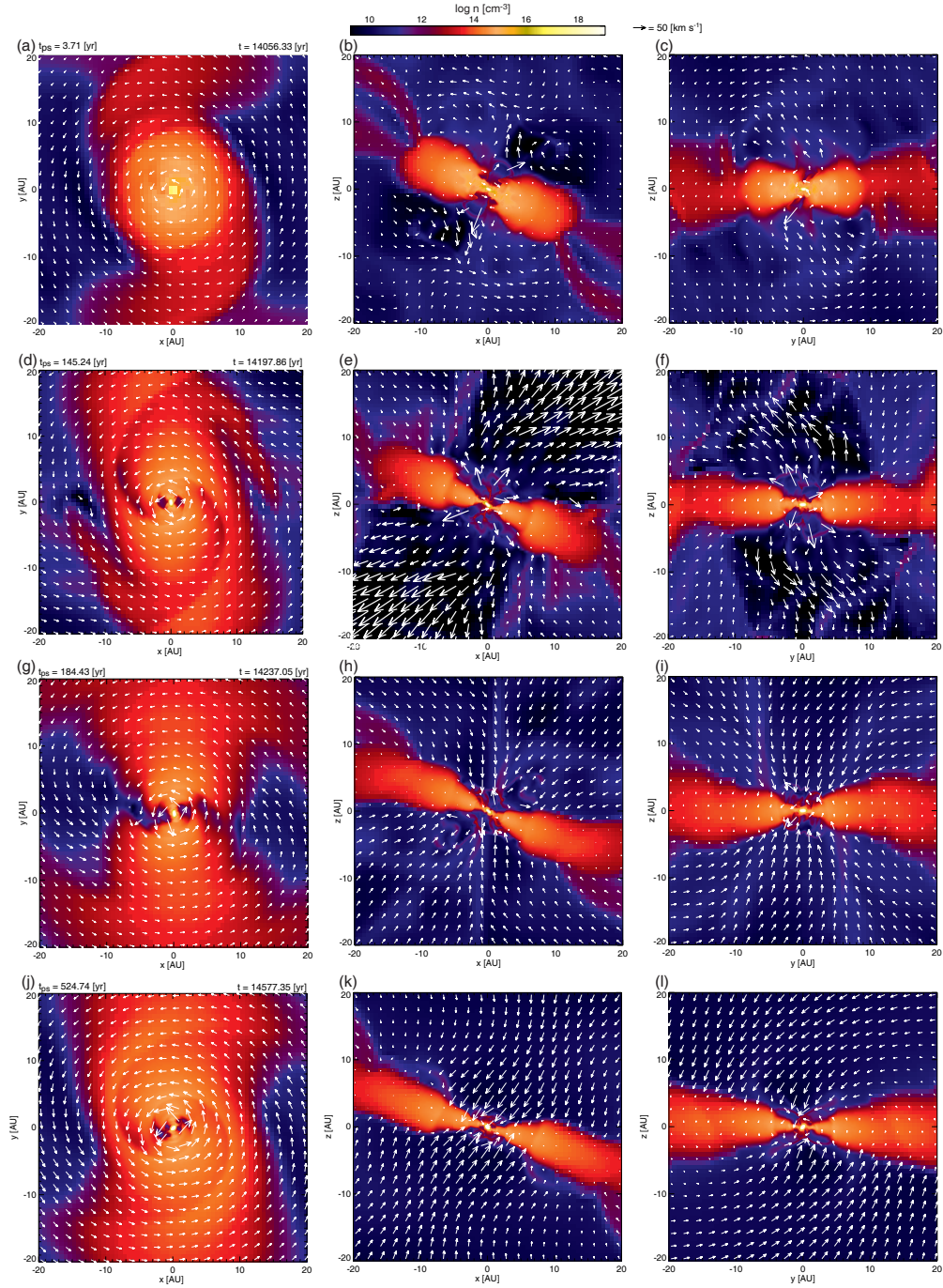


Figure 3. As Fig. 1 but for FM3 (see also FM3.avi).

the parameters $\mu_0 = 3$ and $\alpha_0 = 0.01$. For this model, no low-velocity outflow appears before protostar formation (Papers I and III). A cocoon-like structure can be confirmed just after protostar formation in DM3 (Fig. 1c) and EM3 (Fig. 2c), while no such structure is seen in FM3 (Fig. 3c). After protostar formation, a high-velocity jet also begins to appear for this model, as seen in Figures 3e and f. However, the jet rapidly weakens and disappears at $t_{ps} \sim 160$ yr (Fig. 3h). Then, the jet sometimes appears near the protostar, but does not

MNRAS 000, 1–?? (2020)

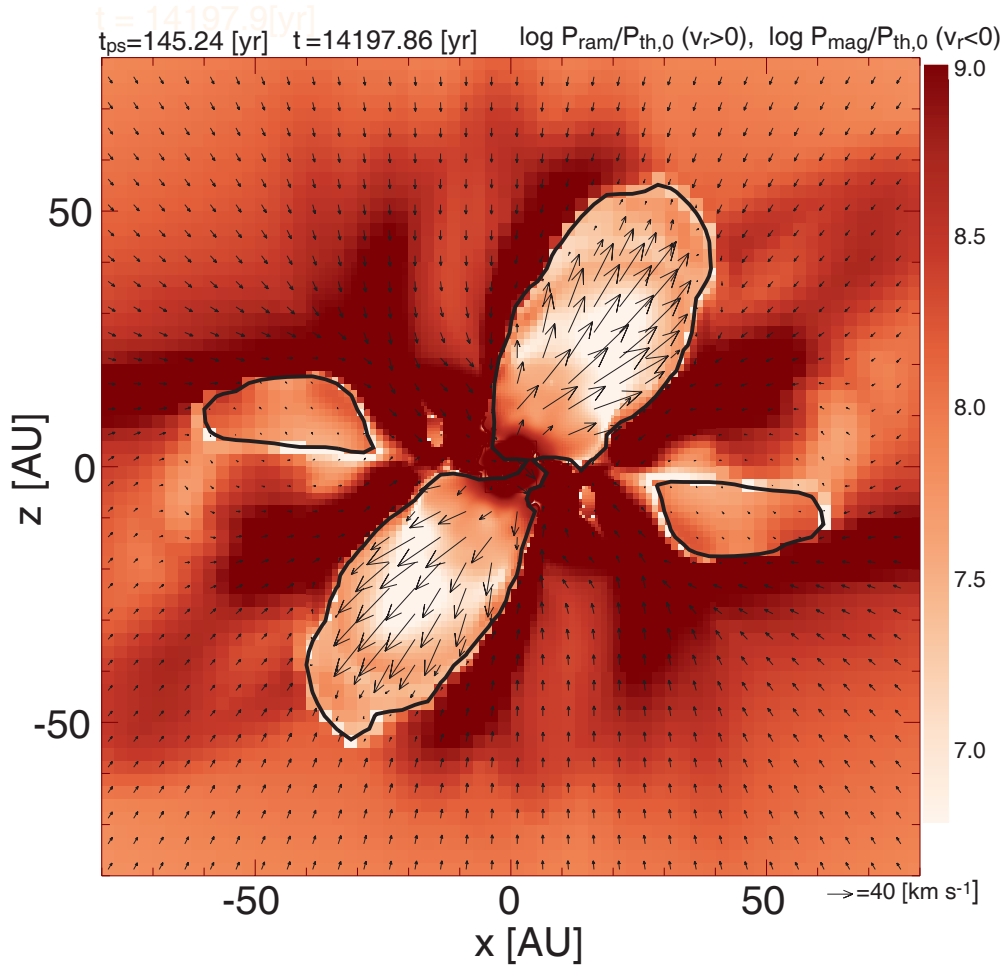


Figure 4. Ram and magnetic pressures on the $y = 0$ plane for FM3. The ram pressure is plotted outside the outflow and the magnetic pressure is plotted inside the outflow. Both the ram ($P_{\text{ram}}/P_{\text{th},0}$) and magnetic ($P_{\text{mag}}/P_{\text{th},0}$) pressures are normalized by the initial thermal pressure at the center of the cloud $P_{\text{th},0}$. The boundary between the outflow ($v_r > 0$) and infalling envelope ($v_r < 0$) is plotted by the black solid curve. The arrows represent the velocity at each point. The elapsed time after protostar formation t_{ps} and that after the cloud begins to collapse t are described in each panel.

grow sufficiently by the end of the simulation. On the other hand, the disk-like structure grows with time (see the middle panels of Fig. 2). At the end of the simulation, we cannot see any sign of mass ejection (Figs. 3*k* and *l*).

For FM3, the ram (outside the jet) and magnetic (inside the jet) pressures when the jet is decaying (or shrinking) are plotted in Figure 4. The figure indicates that the ram pressure in the envelope (or outside the jet) is larger than the magnetic pressure inside the jet. In addition, the jet velocity rapidly decreases near the boundary between the jet and infalling envelope. Thus, it is expected that a high ram pressure suppresses the growth of the jet at this epoch, which is also seen in the case of decaying low-velocity outflow (Paper I and III).

Figure 5 shows the time sequence of the structure in a three-dimensional view for DM3 (upper panels) and FM3 (lower panels). It should be noted that since the time sequence

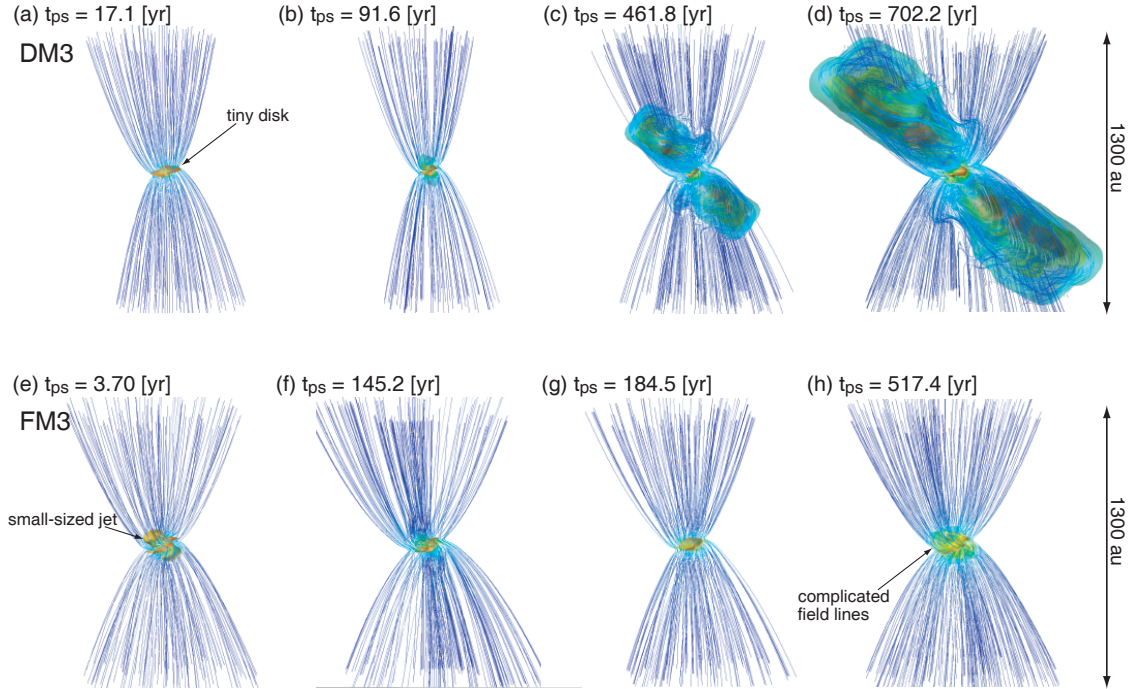


Figure 5. Three dimensional view of DM3 (upper panels) and FM3 (lower panels) at four different epochs. In each panel, the blue lines are magnetic field lines and the central orange region corresponds to the high density region (iso-density surface of 10^{12}cm^{-3}). The outflowing region with $v_r > 0$ is plotted by the nested color surfaces.

for EM3 is essentially the same as FM3, EM3 is omitted from Figure 5. In DM3, we can confirm a tiny disk-like structure at the center and hourglass shaped magnetic field lines in the whole region at the early mass accretion stages (Figs. 5a and b). For this model, the outflow gradually grows with time and the magnetic field lines around the protostar are disturbed by the outflow (Figs. 5c and d). In Figure 5d, the high-velocity component (jet) colored yellow and orange is enclosed by the low-velocity component (outflow) colored blue. The high-velocity jet, which is embedded in the low-velocity component, has a knotty structure that is caused by the episodic mass ejection. At the end of the simulation, the outflow structure has a size of > 1000 au.

On the other hand, in FM3 (Fig. 5 lower panels), although an hourglass configuration of the magnetic field lines can be confirmed, no large scale outflow (either low-velocity outflow or high-velocity jet) appears. In Figure 5h, the magnetic field lines around the protostar are complicated, while we cannot confirm the structure of (large scale) outflow. Figure 5 shows the apparent structural difference between DM3 (upper panels) and FM3 (lower panels).

Figure 6 shows snapshots at $t_{\text{ps}} \sim 500$ yr after protostar formation for all the models having $\mu_0 = 3$. In the figure, the high-velocity jet and low-velocity outflow are sustained for at least $\gtrsim 500$ yr in AM3, BM3, CM3 and DM3, while no mass ejection occurs in EM3 and FM3

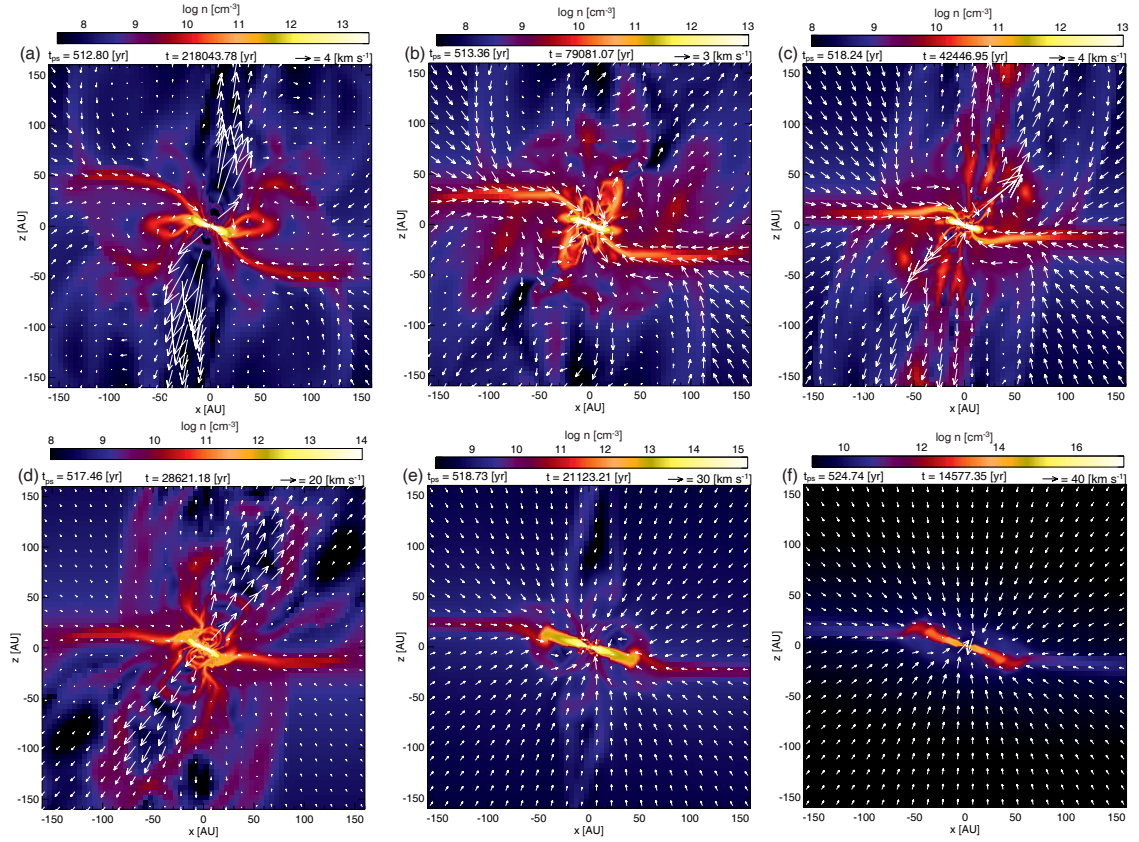


Figure 6. Density (color) and velocity (arrows) distributions on the $y = 0$ plane at $t_{\text{ps}} \sim 500$ yr for AM3 (a), BM3 (b), CM3 (c), DM3 (d), EM3 (e) and FM3 (f). The elapsed time t_{ps} after protostar formation and that t after the beginning of cloud collapse are described in the upper part of each panel.

at the same epoch. In AM3, BM3, CM3 and DM3, although the high-velocity jet extends roughly from northeast to southwest, there is a slight difference in directions between the low-velocity outflow and the high-velocity jet. Especially, the jet axis is somewhat inclined from the outflow axis in CM3 (Fig. 3c), which is also seen in a recent observation (Matsushita et al. 2019). The misalignment between the high- and low-velocity outflows is caused by the warp of the disk (for details, see Hirano & Machida 2019; Machida, Hirano, & Kitta 2020). For EM3 (Fig. 6e) and FM3 (Fig. 6f), the disk normal is also somewhat inclined from the z -axis because the initial rotation axis is set to be inclined from the z -axis toward the x -axis. Figure 6 indicates that the structure around the protostar differs considerably depending on the parameter α_0 or the mass accretion rate (for details, see below).

The time evolution of the outflow length for the models having $\mu_0 = 3$ is plotted in Figure 7, in which the outflowing gas is identified with $v_r > v_{\text{thr}}$ and $v_{\text{thr}} = 1 \text{ km s}^{-1}$ is adopted. I confirmed that the outflow physical quantities do not significantly depend on v_{thr} in the range of $0 < v_{\text{thr}} < 3 \text{ km s}^{-1}$. The figure indicates that the size of the outflow increases with time and reaches $\sim 700\text{--}1000$ au for about 600 yr after protostar formation in AM3, BM3, CM3

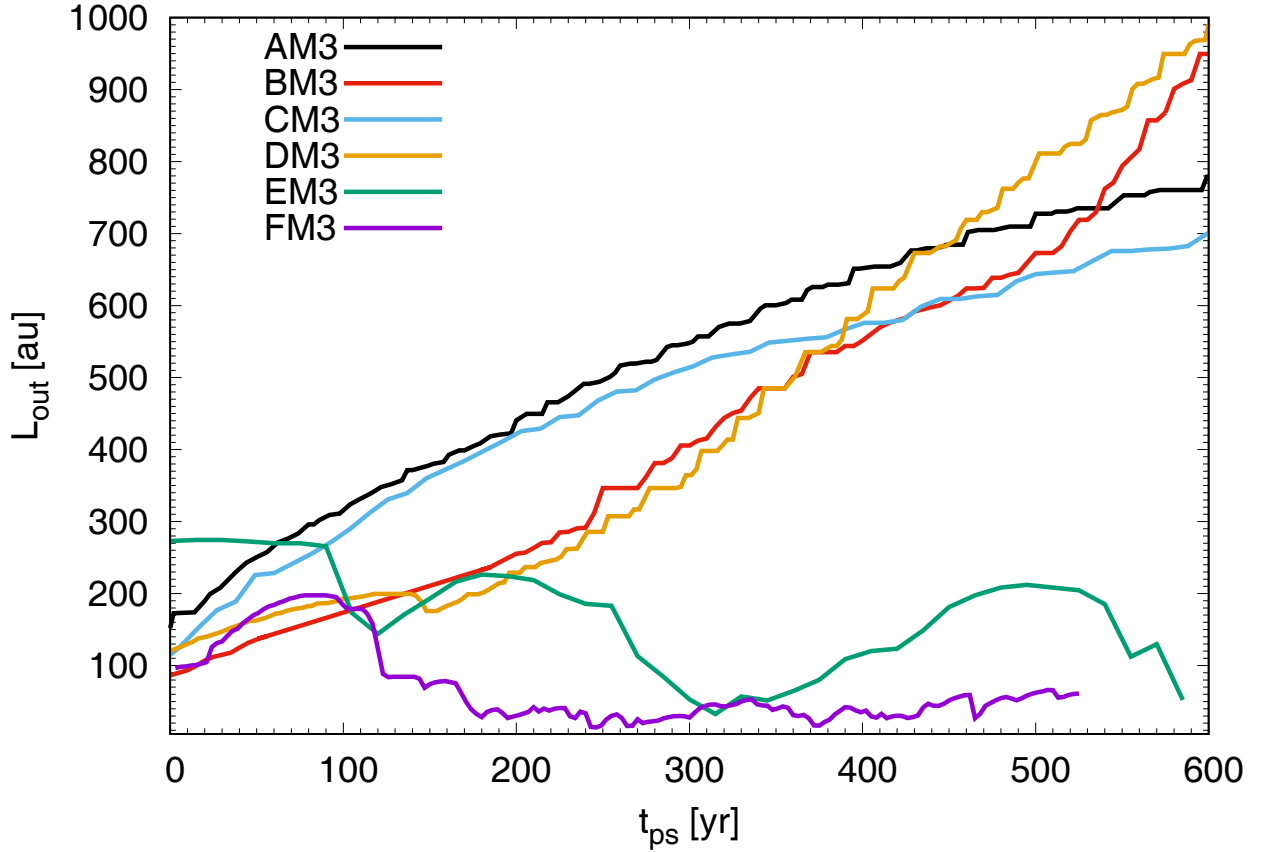


Figure 7. Outflow length against the elapsed time after protostar formation for AM3, BM3, CM3, DM3, EM3 and FM3.

and DM3. On the other hand, in EM3 and FM3, the outflow does not grow after protostar formation. In these models, the outflow length repeatedly increases and decreases within the range of $\lesssim 200$ au, indicating that the high-velocity jet and low-velocity outflow appearing episodically around the protostar lose their power before the outflow grows sufficiently. The suppression of the outflow due to the ram pressure of the infalling envelope was elaborately investigated in Paper III (see also Fig. 4).

To confirm the velocity component of the outflow, we plot the mass $\Delta M_{\text{out}}(v_{\text{out}})$ and momentum flux $\Delta F_{\text{out}}(v_{\text{out}})$ of the outflowing gas at each velocity component (or velocity bin), estimated as

$$\Delta M_{\text{out}}(v_{\text{out}}) = \int_{v_{\text{out}} - \Delta v}^{v_{\text{out}} + \Delta v} \rho dV, \quad (2)$$

$$\Delta F_{\text{out}}(v_{\text{out}}) = \frac{\Delta P(v_{\text{out}})}{t_{\text{ps}}}, \quad (3)$$

where $\Delta v = 2.5 \text{ km s}^{-1}$ was adopted, against the outflow velocity at $t_{\text{ps}} \simeq 500 - 600 \text{ yr}$ in Figure 8. In equation (3), the outflow momentum $\Delta P_{\text{out}}(v_{\text{out}})$ at each velocity component is

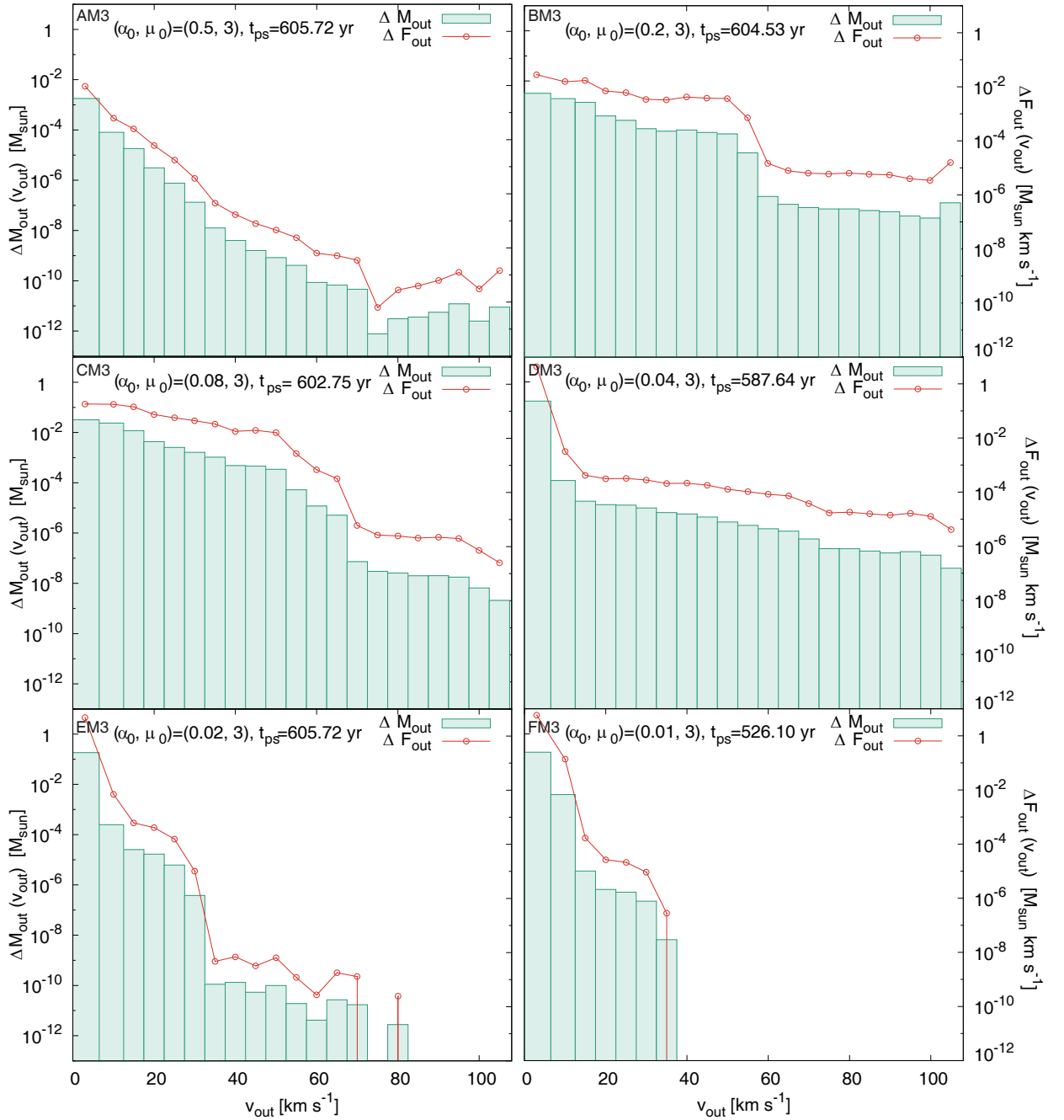


Figure 8. Histogram of outflow mass ΔM_{out} (left axis) and momentum flux ΔF_{out} (right axis) against the outflow velocity v_{out} for AM3, BM3, CM3, DM3, EM3 and FM3. The model name, parameters (α_0 and μ_0) and elapsed time (t_{ps}) are described in each panel.

calculated as

$$\Delta P_{\text{out}}(v_{\text{out}}) = \int_{v_{\text{out}} - \Delta v}^{v_{\text{out}} + \Delta v} \rho |\mathbf{v}| dV. \quad (4)$$

Note that, in equations (2)–(4), the quantities are integrated only in the outflowing region of $v_r > v_{\text{thr}}$. In AM3, BM3, CM3 and DM3, although the low-velocity components dominate the high-velocity components, there exists a non-negligible amount of outflowing mass and mo-

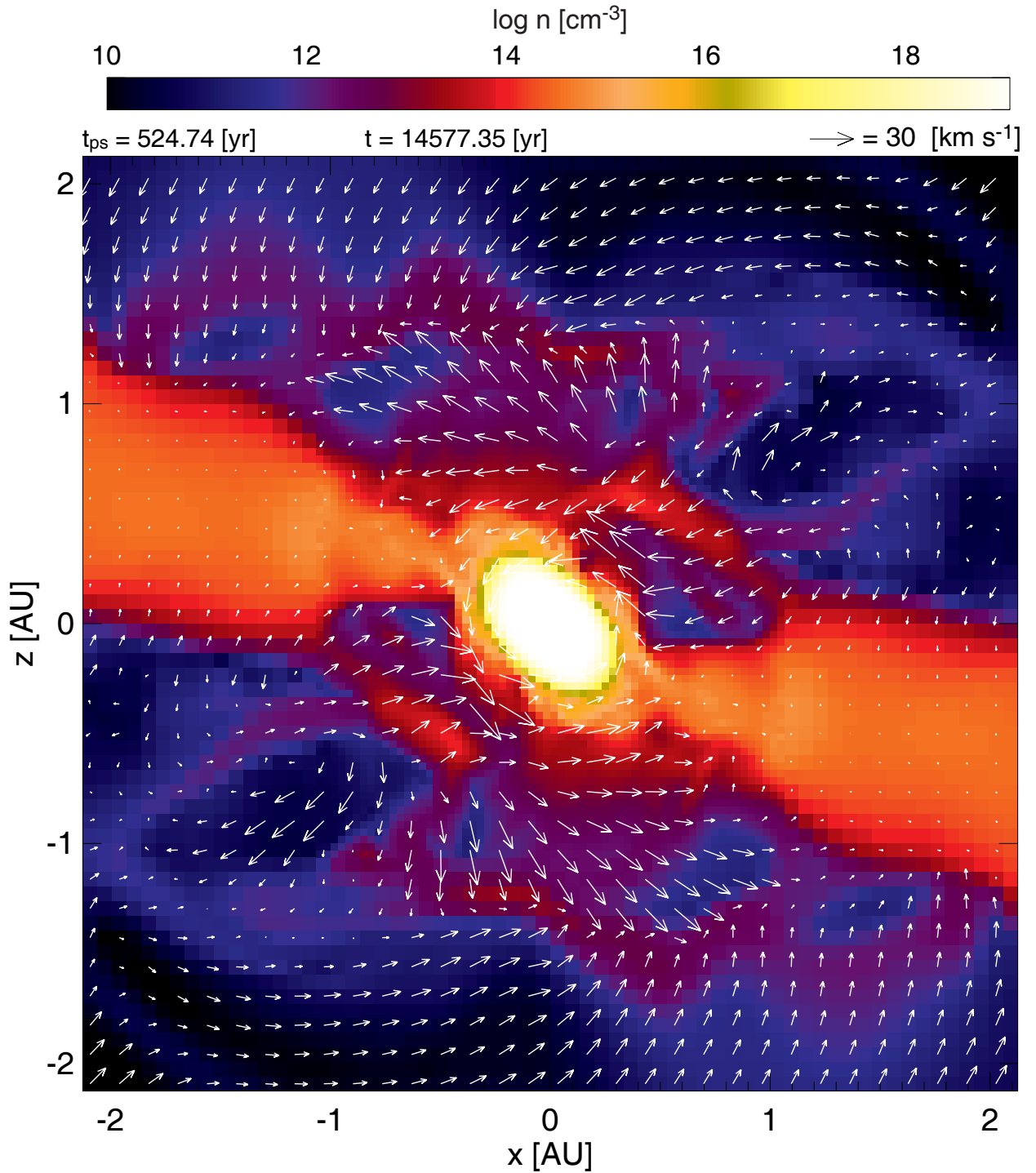


Figure 9. Density (color) and velocity (arrows) distributions on the $y = 0$ plane for FM3 at the same epoch as in Fig. 3k. The elapsed time t_{ps} after protostar formation and that t after the beginning of the cloud collapse are described.

momentum flux in the high-velocity components. For these models, although the distributions of ΔM_{out} and ΔF_{out} show time variability, neither the low- or high-velocity components disappear at any epoch. A similar distribution to these models can be confirmed in the low-mass star formation case (Saiki & Machida 2020).

On the other hand, no high-velocity component exists in EM3 and FM3 in Figure 8. In EM3, the mass and momentum flux of the outflowing gas rapidly decrease around $v_{\text{out}} \simeq 30 \text{ km s}^{-1}$ and disappear in the range $v_{\text{out}} > 80 \text{ km s}^{-1}$. In FM3, there is no high-velocity component for $v_{\text{out}} > 40 \text{ km s}^{-1}$. Thus, it is clear that no high-velocity jets appear in EM3 and FM3. In these models, it seems that there are low-velocity outflow components. However, in fact, the low-velocity components can be identified only around the region very close to the protostar and there is no evolved low-velocity outflow by the end of the simulation, as seen in Figures 2 and 3. To confirm the region around the protostar, a close-up view of Figure 3*k* is plotted in Figure 9. We cannot clearly identify the outflow in a large scale (Figs. 3*k* and 6*f*), while we can confirm the outflow around the protostar in a small scale (Fig. 9). A major component of the outflow stays within $\sim 2 \text{ au}$ and does not grow by the end of the simulation for FM3 (and EM3).

Figure 10 shows the protostellar mass (Fig. 10*a*), the mass infall rate (Fig. 10*b*) and the ratio of outflow to inflow rate (Fig. 10*c*) against the elapsed time after protostar formation. The protostellar mass is estimated as being the region with $n > n_{\text{ps}}$, where $n_{\text{ps}} = 10^{18} \text{ cm}^{-3}$ is adopted (Machida & Basu 2019). As seen in Figure 10*a*, the protostellar mass increases as α_0 decreases, because the mass accretion rate or infall rate depends on α_0 , as explained in Paper I. The infall rate is estimated by integrating over the gas with $v_r < 0$ passing through a spherical surface with a radius of 1 au as

$$\dot{M}_{\text{in}} = \int^{v_r < 0} \rho v_r dS. \quad (5)$$

In the analytical estimate, the mass accretion (or infall) rate is proportional to $\alpha_0^{-3/2}$ (for details, see Paper I). Thus, it is natural that the mass accretion rate for models with small α_0 is higher than that for the model with large α_0 .

We can see a significant difference (or gap) between DM3 and EM3 in Figures 10*a* and *b* caused by the lack of outflow in EM3 and FM3. Figure 10*c* shows the ratio of outflow to inflow rate, in which the outflow rate,

$$\dot{M}_{\text{out}} = \int^{v_r > 0} \rho v_r dS, \quad (6)$$

is estimated using the same spherical surface as used in estimating the inflow rate (\dot{M}_{in}). In the panel, we can also see a significant difference between the models with and without outflow. As shown in Figures 6 and 7, the outflow grows in AM3, BM3, CM3 and DM3, while it is not evolved in EM3 and FM3.

For AM3, BM3, CM3 and DM3, the outflow rate is comparable or larger than the infall

rate, as seen in Paper I. The infall and outflow rates are estimated at a radius of 1 au and the protostar has a size of 0.01–0.2 au. Thus, a part of the infalling gas is swept by the high-velocity jet driven near the protostar. As a result, the mass of the outflowing gas can dominate that of the infalling gas (see also Papers I and II). Since not all the infalling gas is ejected by the high-velocity jet, the protostellar mass gradually increases even when strong mass ejection occurs around the protostar (AM3, BM3, CM3 and DM3).

On the other hand, the ratio ($\dot{M}_{\text{out}}/\dot{M}_{\text{in}}$) rapidly decreases in EM3 and FM3 (Fig. 10c). Since the mass inflow rate is high in such models, the decrease of the ratio indicates that the mass outflow rate rapidly decreases. Thus, the infalling gas is not significantly disrupted by the high-velocity jet in these models. Therefore, a high infall rate (Fig. 10b) and high-mass protostar tends to be realized (Fig. 10c) in these models. Figure 10a indicates that the outflow affects the mass growth of the protostar.

3.2 Parameter Dependence

While we considered the cloud evolution for the models with an initially strong magnetic field with $\mu_0 = 3$ in §3.1, in this subsection, the cloud evolution for all models is described. Figure 11 shows the outflow length against the elapsed time after protostar formation for all the models listed in Table 1. In the figure, for the models with $\alpha_0 = 0.5$ (Fig. 11a), 0.2 (Fig. 11b) and 0.08 (Fig. 11c), the outflow length continues to increase only when the initial magnetic field is as strong as $\mu_0 = 3$. Figures 11a–c also show that the outflow lengths for the models with $\mu_0 \geq 5$ stay within ~ 200 au by the end of the simulation². Thus, neither the low-velocity outflow nor high-velocity jet sufficiently evolve in these models. These models ($\alpha_0 = 0.5, 0.2$ and 0.08) have a relatively low mass accretion rate of $\dot{M} \lesssim 5 \times 10^{-5} M_{\odot} \text{ yr}^{-1}$ (Fig. 10b).

The models with $\alpha_0 = 0.04$ (Fig. 11d) are an exception. As seen in Figure 10b, the model with $\alpha_0 = 0.04$, DM3, has an intermediate mass accretion rate of $\sim 10^{-4} M_{\odot} \text{ yr}^{-1}$. In Figure 11d, although the outflow growth rates are different among the models, the outflows continue to evolve up to the end of the simulation in all the models (DM3, MD5, DM10 and DM20).

² A sharp drop of AM20 at $t_{\text{ps}} \sim 200$ yr seen in Fig. 11a is due to the outflow identification criteria. As described in §3.1, I defined the outflow as the outflowing gas having $v_r \geq 1 \text{ km s}^{-1}$. The head of the outflow gradually decelerates, while the mass ejection episodically occurs. Thus, the inner outflowing gas is identified as the head of the outflow after the forward outflow decelerates to $v_r < 1 \text{ km s}^{-1}$, which causes the sharp drop of the outflow length.

For the models with $\alpha_0 = 0.02$ and 0.01 (EM3, EM5, EM10, FM3, FM5, FM10), which have a high mass accretion rate ($> 10^{-4} M_\odot \text{ yr}^{-1}$), the low-velocity outflow and high-velocity jet are not very active. In Figures 11*e* and *f*, the outflow lengths for these models oscillate within 300 au. Thus, almost none of the models plotted in these panels show a successful growth of the outflow. Among the models, although EM5 and FM10 show continuous growth of the outflow, their lengths are much smaller than those of the successful growth models (AM3, BM3, CM3, DM3).

Figure 12 shows the outflow momentum P_{out} , calculated as

$$P_{\text{out}} = \int^{v_r > v_{\text{thr}}} \rho |\mathbf{v}| dV, \quad (7)$$

for all model. The trend of the outflow momentum seen in Figure 12 is similar to that in Figure 11. In Figure 12*a-c* (models with $\alpha_0 = 0.5, 0.2$ and 0.08), the outflow momenta for the models with $\mu_0 = 3$ are much larger than those for models with $\mu_0 \geq 5$. For the models with $\alpha_0 = 0.04$ (DM3, DM5, DM10, DM20; Fig. 12*d*), the difference in the outflow momenta among the models is not very large, because the outflow in these models continues to grow up to the end of the simulation, as shown in Figure 11. However, the outflow momentum is larger in the model with a stronger magnetic field than that with a weaker magnetic field at the end of the simulation.

For the models with high mass accretion ($\alpha_0 = 0.02$ and 0.01 ; Figs. 12*e* and *f*), the outflow momenta for the models with the strongest magnetic field (EM3, FM3) are much larger than those with weak magnetic fields (EM5, EM10, FM5, FM10). However, Figures 11*e* and *f* indicate that the outflow does not sufficiently grow and the outflowing gas stays near the protostar for the models with $\mu_0 = 3$ (EM3, FM3). Thus, the large momenta for these models is due to the dense gas staying around the protostar (see Figs 2, 3 and 9).

In addition, Figures 11*e* and *f* also indicate that the outflow can grow in models EM5 and FM10. However, the outflow momenta for models EM5 and FM10 are about one order of magnitude smaller than those for the models with $\mu_0 = 3$ (EM3, FM3). Thus, it is considered that only a very weak outflow can evolve in such models.

Figure 13 shows the three dimensional structure at the end of the simulation for all the models plotted on the μ_0 - α_0 parameter plane. The box size (260 au) is the same in each panel. As described in §2, the parameter μ_0 corresponds to the magnetic field strength of the prestellar cloud, while the parameter α_0 controls the mass accretion rate onto the central region. In the figure, the models are classified into three categories as strong, weak and no

jet cases (or models), with red, orange and white backgrounds, respectively. Although it is difficult to determine the jet strength (strong or weak jet), I used the momentum (Fig. 12) and length growth (Fig. 11) of the outflowing gas as indicators of the jet strength. Note that the physical quantities of the outflowing gas such as outflow mass, momentum and kinetic energy increase as the mass accretion rate increases or the parameter α_0 decreases (for details, see Papers I and II). Thus, I only compared the outflow physical quantities (Figs. 11 and 12) for the models with the same α_0 .

In Figure 13, the strong jet models (red background) are distributed only in the lower left, indicating that a strong (high-velocity) jet appears only when both conditions of strong magnetic field and low-mass accretion rate are realized. A clear bipolar jet structure can be seen in the models in red panels. In the models located in the lower center and right (panels without background color), although the magnetic field lines are slightly entangled around the center, we cannot confirm a clear jet structure.

We can confirm a jet (or outflow) structure in all the models with an intermediate accretion rate ($\alpha_0 = 0.04$ and 0.08 models) in Figure 13. A clear bipolar structure can be seen in the models with $\mu_0 = 3$. On the other hand, the structures of the jet (or outflow) are highly complicated or small for the models with $\mu_0 \geq 5$. For the high mass accretion cases with $\alpha_0 = 0.01$ and 0.02 , the models with the strongest magnetic fields ($\mu_0 = 3$) do not show a jet structure. Meanwhile, a bipolar jet-like structure can be seen in the models with $(\alpha_0, \mu_0) = (0.02, 5)$ and $(0.01, 10)$.

In summary, the models with a strong magnetic field and/or a low-mass accretion rate always show a clear jet structure. The models with a high-mass accretion rate and a weak magnetic field do not always show a bipolar jet and outflow structure. Even if an outflow appears in such models, the momentum and size of the outflow are very small.

4 DISCUSSION

In the star forming regions, protostellar jets are observed as proof of star formation. Jet and outflow driving in the star formation process has been investigated in core collapse simulations. However, in many simulations, the jet driving was investigated only in a limited parameter range (Tomida et al. 2013). Clouds with strong magnetic fields and low-mass accretion rates are usually chosen as the initial condition of core collapse simulations to investigate a high-velocity flow driven by the protostar (Tomida et al. 2013; Machida 2014;

Machida & Basu 2019)³. The difference in the initial condition may cause different outcomes (Vaytet et al. 2018; Wurster, Bate, & Price 2018). Thus, we need to perform core collapse simulations with various initial conditions to investigate whether protostellar jets universally appear in the star formation process. This study focuses on jet driving with different star-forming environments. In other words, I especially included jet driving in clouds with weak magnetic fields and a high mass accretion rates in the investigation. Another purpose of this study is to investigate whether a jet driven near the protostar can help to drive a low-velocity and wide-angle outflow, based on the finding in Paper III that the outflow fails to be driven with a weak magnetic field and/or a high mass accretion rate.

Figure 14 shows the outcomes of this study and Paper III. In each panel, the outcome of this study is presented in the upper left, while that of Paper III is in the lower right. The model names used in this study are the same as those in Paper III when the parameters α_0 and μ_0 are the same. The initial condition is almost the same between the two studies. The difference in the initial condition is the angle between the magnetic and angular momentum vectors of the prestellar cloud θ_0 , as described in §2. The angle $\theta_0 = 0$ was adopted in Paper III, while $\theta_0 = 20^\circ$ is used in this study. Thus, the initial magnetic field and angular momentum vector are aligned in Paper III, while they are misaligned in this study. In addition, the integration time t_{end} and spatial resolution h are different between this study ($t_{\text{end}} \sim 500$ yr and $h = 7.9 \times 10^{-3}$ au) and Paper III ($t_{\text{end}} \sim 10^4$ yr and $h = 0.62$ au). Hence, it is difficult to fairly compare the outcomes between them. However, we cannot realize a long-term cloud evolution with a high-spatial resolution. Thus, it would be valuable to overview the results between them in order to further understand the driving mechanism of low- and high-velocity flows. In this section, I discuss the possibility of jet and outflow driving in the clouds with different magnetic field strengths and mass accretion rates using the results in Paper III and this study.

In §3, all the outflowing gas observed in this study is referred to as outflow, with the outflow being composed of both high-velocity (or high-velocity jet) and low-velocity (low-velocity outflow) components. Here, I redefine the terms ‘jet’ and ‘outflow’, *used only in the*

³ It should be noted that, for the low-mass star formation case, Bate, Tricco, & Price (2014) investigated the jet driving in the clouds with different magnetic field strengths ($\mu_0 = 5, 10, 20, 100$) resolving the protostar. Although they calculated the jet driving only for $\sim 2 - 3$ yr, the high-velocity jet extends to ~ 3 au from the protostar in the models with $\mu_0 = 5, 10$, and 20. Note that, in their study, no jet appears in the model with $\mu_0 = 100$. I confirmed that, in my simulations, the jet appears and is sustained at least in the very early phase for the model with $\mu_0 = 3, 5, 10$ and 20 (Fig. 11).

following paragraphs in this section, to distinguish the terms used for the outflow between this study and Paper III. In this section, I refer to the outflow as the outgoing flow observed in *Paper III*, while I call the jet the outgoing flows observed *in this study*. In addition, referring to Figures 11–13, I call a jet with a large momentum a strong jet and one with small momentum a weak jet. Furthermore, in this study, since the low-velocity component appears with the high-velocity jet (or high-velocity component), as seen in Figure 8, I call the low-velocity component of a jet the low-velocity outflow (or low-velocity component) and the high-velocity flow the high-velocity jet (high-velocity component). As seen in Figure 8, there is no clear boundary between a high-velocity jet and low-velocity outflow. Thus, it is difficult to separate low-velocity outflow from a high-velocity jet. The low-velocity outflow may be directly driven by the disk outer edge, as explain in Papers I–III. Alternatively, it may be entrained by the high-velocity component when the high-velocity jet appears. In the present study, I do not consider the driving mechanism of the low-velocity components appearing in this study, as this is outside the scope of this study.

First, I focus on the models with $\alpha_0 = 0.2$ and 0.5 (the fifth and sixth lines in Fig. 14; models AM3, AM5, AM10, AM20, BM3, BM5, BM10, BM20), which have a low mass accretion rate (Fig. 10) and would form low mass stars. Figure 14 shows that both outflow and jets appear only in AM3 and BM3, which have the strongest magnetic fields ($\mu_0 = 3$). For these models, the outflow appears without resolving the jet driving region (Paper III). The jet also appears as described in §3. Thus, it is considered that a high-velocity jet and low-velocity outflow are driven at different radii in the circumstellar disk, as expected from past core collapse simulations (Tomida et al. 2013; Machida & Basu 2019). On the other hand, when the magnetic field is not strong ($\mu_0 \geq 5$; AM5, AM10, AM20, BM5, BM10, BM20), jets do not appear. In Figure 14, ‘Delayed Outflow’ refers to the case where a (weak) outflow begins to grow only in the late accretion phase, just before the infalling envelope dissipates (Paper III). Also, for BM10 and BM20, neither jets (this study) nor outflow (Paper III) appear. Thus, for these models, the outflow and jet would not play a significant role by the end of the mass accretion phase. Note that since the jet driving was calculated only for ~ 500 yr in the main accretion phase with a high spatial resolution, I cannot clearly state that the jet driving is completely suppressed by the end of the mass accretion phase. However, since no jet appears, it cannot help to drive the low-velocity outflow, at least, in the early main accretion phase.

Next, I describe the models with $\alpha_0 = 0.04$ and 0.08 (the third and fourth lines in Fig. 14;

CM3, CM5, CM10, CM20, DM3, DM5, DM10, DM20), which have moderate mass accretion rates (Fig. 11) and would form intermediate mass stars. Even for these models, both the jet and outflow appear only when the magnetic field is as strong as $\mu_0 = 3$. Thus, as described above, the jet and outflow are expected to be driven at different radii of the circumstellar disk. The difference between low-mass ($\alpha_0 = 0.2$ and 0.5) and intermediate-mass ($\alpha = 0.04$ and 0.08) stars can be seen in the models with weak magnetic fields. When the magnetic field is as weak as $\mu \geq 5$, neither jets nor outflow appear in the early accretion phase for the low-mass star formation cases. On the other hand, a weak jet appears for all models with $\mu_0 \geq 5$ (CM5, CM10, CM20, DM5, DM10, DM20) for intermediate star formation cases. As shown in Figure 8, in addition to the high-velocity component, the low-velocity component exists when a jet appears (Fig. 8). Thus, a part of the outflowing gas would be entrained by the high-velocity jet. Alternatively, the jet may alleviate the ram pressure barrier which suppresses the growth of the low-velocity outflow and promotes outflow directly driven by the outer disk region. However, the momentum of the outflowing gas in these weak jet models is not as large as that in strong jet models (Fig. 12). Thus, the contribution of the jet to the low-velocity outflow is limited.

Finally, I describe the models with $\alpha_0 = 0.01$ and 0.02 (the first and second lines in Fig. 14; EM3, EM5, EM10, FM3, DM5, FM10) which have high mass accretion rates (Fig. 11) and would form high mass stars. No strong jets appear in these models, while only EM3 shows an outflow after protostar formation. Model EM3 is a special case of all the models listed in Table 1, because only this model shows a low-velocity outflow (Paper III) without showing a jet (this study). In Paper III, the outflow begins to grow about 1,000 yr after protostar formation in model EM3. Thus, the protostellar system drives only the low-velocity outflow without the high-velocity component, which may explain the observation of Hirota et al. (2017).

For EM5 and FM10, a weak jet appears in the early mass accretion phase (this study), while the outflow appears in the later accretion phase (Paper III). Meanwhile, for FM3 and FM5, the outflow appears in the late accretion phase (Paper III), while no jet appears (this study). For EM10, neither jet nor outflow appear in either study. Thus, it is expected that, for these models (EM5, EM10, FM3, FM5, FM10), jets and outflow do not significantly affect the star formation process throughout the main accretion phase. In addition, in the models with $\alpha_0 = 0.01$ and 0.02 , jets would not greatly contribute to driving the low-velocity outflow because of a lack of strong jets.

The protostellar outflow is considered to have a significant impact on star formation. However, Figure 14 indicates that there are various star formation scenarios (with and without jets and outflow) dependent on the initial prestellar cloud’s magnetic field strength and intrinsic mass accretion rate.

Finally, I again emphasize the caveat in the above discussion. In Papers I-III, I prepared the aligned models, in which the rotation axis of the prestellar cloud is aligned with the global magnetic field. Since such a setting is not very realistic, I prepared the misaligned models in this study (see §2). In addition, although the protostar was spatially resolved, I could not follow the long-term evolution of the jet. For further understanding of the jet and outflow driving, future studies should focus on the long-term evolution of the jet resolving the protostar with the parameters μ_0 , α_0 and θ_0 .

5 SUMMARY

In this study, I investigated jet driving in clouds with different magnetic field strengths and intrinsic mass accretion rates using numerical simulations. I found that a high-velocity jet appears near the protostar and is sustained for a long time only when the magnetic field strength of the prestellar cloud is as strong as $\mu_0 \leq 3$ and the mass accretion rate onto the central region is as low as $\dot{M} < 10^{-4} M_\odot \text{yr}^{-1}$. When strongly magnetized clouds ($\mu_0 = 3$) have a mass accretion rate higher than $\dot{M} > 10^{-4} M_\odot \text{yr}^{-1}$, a high-velocity jet can be driven near the protostar in the early mass accretion phase. However, the jet does not grow sufficiently and quickly disappears. On the other hand, when the magnetic field of the star-forming cloud is weak, a jet sometimes appears for a mass accretion rate higher than $\dot{M} > 10^{-5} M_\odot \text{yr}^{-1}$. In this case, a low-velocity component also appears in conjunction with the high-velocity jet. However, the outflow momentum in weakly magnetized clouds is much lower than that in strongly magnetized clouds. Thus, a high-velocity jet does not significantly contribute to driving a low-velocity outflow. This study indicates that a protostellar outflow cannot significantly contribute to the star formation process when the magnetic field strength of the star-forming cloud is weak.

ACKNOWLEDGEMENTS

This research used the computational resources of the HPCI system provided by the Cyber Science Center at Tohoku University and the Cybermedia Center at Osaka University

(Project ID: hp200004, hp210004). Simulations reported in this paper were also performed by 2019 and 2020 Koubo Kadai on Earth Simulator (NEC SX-ACE) at JAMSTEC. The present study was supported by JSPS KAKENHI Grant (JP17H06360, JP17K0538faa7, JP17KK0096, JP21H00046, JP21K03617: MNM).

DATA AVAILABILITY

The data underlying this article are available in the article and in its online supplementary material.

REFERENCES

- Alves F. O., Girart J. M., Caselli P., Franco G. A. P., Zhao B., Vlemmings W. H. T., Evans M. G., et al., 2017, *A&A*, 603, L3. doi:10.1051/0004-6361/201731077
- Aso Y., Hirano N., Aikawa Y., Machida M. N., Ohashi N., Saito M., Takakuwa S., et al., 2019, *ApJ*, 887, 209. doi:10.3847/1538-4357/ab5284
- Arce H. G., Shepherd D., Gueth F., Lee C.-F., Bachiller R., Rosen A., Beuther H., 2007, *prpl.conf*, 245
- Bate M. R., Tricco T. S., Price D. J., 2014, *MNRAS*, 437, 77. doi:10.1093/mnras/stt1865
- Bjerkeli P., van der Wiel M. H. D., Harsono D., Ramsey J. P., Jørgensen J. K., 2016, *Natur*, 540, 406. doi:10.1038/nature20600
- Banerjee R., Pudritz R. E., 2006, *ApJ*, 641, 949. doi:10.1086/500496
- Blandford R. D., Payne D. G., 1982, *MNRAS*, 199, 883. doi:10.1093/mnras/199.4.883
- Ciardi A., Hennebelle P., 2010, *MNRAS*, 409, L39. doi:10.1111/j.1745-3933.2010.00942.x
- de Valon A., Dougados C., Cabrit S., Louvet F., Zapata L. A., Mardones D., 2020, *A&A*, 634, L12. doi:10.1051/0004-6361/201936950
- Hennebelle P., Fromang S., 2008, *A&A*, 477, 9. doi:10.1051/0004-6361:20078309
- Hirano S., Machida M. N., 2019, *MNRAS*, 485, 4667. doi:10.1093/mnras/stz740
- Hirano S., Tsukamoto Y., Basu S., Machida M. N., 2020, *ApJ*, 898, 118. doi:10.3847/1538-4357/ab9f9d
- Hirota T., Machida M. N., Matsushita Y., Motogi K., Matsumoto N., Kim M. K., Burns R. A., et al., 2017, *NatAs*, 1, 0146. doi:10.1038/s41550-017-0146
- Inutsuka S., 2012, *PTEP*, 2012, 01A307. doi:10.1093/ptep/pts024
- Joos M., Hennebelle P., Ciardi A., 2012, *A&A*, 543, A128. doi:10.1051/0004-6361/201118730
- Kölligan A., Kuiper R., 2018, *A&A*, 620, A182. doi:10.1051/0004-6361/201833686
- Lee C.-F., Tabone B., Cabrit S., Codella C., Podio L., Ferreira J., Jacquemin-Ide J., 2021, *ApJL*, 907, L41. doi:10.3847/2041-8213/abda38
- Lewis B. T., Bate M. R., Price D. J., 2015, *MNRAS*, 451, 288. doi:10.1093/mnras/stv957
- Lewis B. T., Bate M. R., 2017, *MNRAS*, 467, 3324. doi:10.1093/mnras/stx271
- Marchand P., Tomida K., Tanaka K. E. I., Commerçon B., Chabrier G., 2020, *ApJ*, 900, 180. doi:10.3847/1538-4357/abad99
- Machida, M. N., Tomisaka, K., & Matsumoto, T. 2004, *MNRAS*, 348, L1
- Machida, M. N., Matsumoto, T., Tomisaka, K., & Hanawa, T. 2005, *MNRAS*, 362, 369
- Machida M. N., Inutsuka S., Matsumoto T., 2006, *ApJL*, 647, L151. doi:10.1086/507179
- Machida M. N., Inutsuka S., Matsumoto T., 2007, *ApJ*, 670, 1198. doi:10.1086/521779
- Machida M. N., Inutsuka S., Matsumoto T., 2008, *ApJ*, 676, 1088. doi:10.1086/528364
- Machida, M. N., Inutsuka, S., & Matsumoto, T. 2010, *ApJ*, 724, 1006

- Machida M. N., Hosokawa T., 2013, MNRAS, 431, 1719. doi:10.1093/mnras/stt291
- Machida M. N., 2014, ApJL, 796, L17. doi:10.1088/2041-8205/796/1/L17
- Machida M. N., Nakamura T., 2015, MNRAS, 448, 1405. doi:10.1093/mnras/stu2633
- Machida M. N., Basu S., 2019, ApJ, 876, 149. doi:10.3847/1538-4357/ab18a7
- Machida M. N., Hosokawa T., 2020a, MNRAS, 499, 4490. doi:10.1093/mnras/staa3139
- Machida M. N., Hirano S., Kitta H., 2020b, MNRAS, 491, 2180. doi:10.1093/mnras/stz3159
- Matsushita Y., Machida M. N., Sakurai Y., Hosokawa T., 2017, MNRAS, 470, 1026. doi:10.1093/mnras/stx893
- Matsushita Y., Sakurai Y., Hosokawa T., Machida M. N., 2018, MNRAS, 475, 391. doi:10.1093/mnras/stx3070
- Matsushita Y., Takahashi S., Machida M. N., Tomisaka K., 2019, ApJ, 871, 221. doi:10.3847/1538-4357/aaf1b6
- Masson J., Chabrier G., Hennebelle P., Vaytet N., Commerçon B., 2016, A&A, 587, A32. doi:10.1051/0004-6361/201526371
- Matzner C. D., McKee C. F., 2000, ApJ, 545, 364. doi:10.1086/317785
- Saiki Y., Machida M. N., 2020, ApJL, 897, L22. doi:10.3847/2041-8213/ab9d86
- Seifried D., Banerjee R., Klessen R. S., Duffin D., Pudritz R. E., 2011, MNRAS, 417, 1054. doi:10.1111/j.1365-2966.2011.19320.x
- Seifried, D., Pudritz, R. E., Banerjee, R., Duffin, D., & Klessen, R. S. 2012, MNRAS, 422, 347
- Tabone B., Raga A., Cabrit S., Pineau des Forêts G., 2018, A&A, 614, A119. doi:10.1051/0004-6361/201732031
- Tanaka, K. E. I., Tan, J. C., & Zhang, Y. 2017, ApJ, 835, 32
- Tanaka, K. E. I., Tan, J. C., Zhang, Y., et al. 2018, ApJ, 861, 68
- Tokuda K., Onishi T., Saigo K., Matsumoto T., Inoue T., Inutsuka S., Fukui Y., et al., 2018, ApJ, 862, 8. doi:10.3847/1538-4357/aac898
- Tomida K., Tomisaka K., Matsumoto T., Hori Y., Okuzumi S., Machida M. N., Saigo K., 2013, ApJ, 763, 6. doi:10.1088/0004-637X/763/1/6
- Tomisaka K., 2000, ApJL, 528, L41. doi:10.1086/312417
- Tomisaka K., 2002, ApJ, 575, 306. doi:10.1086/341133
- Truelove, J. K., Klein, R. I., McKee, C. F., et al. 1997, ApJ, 489, L179
- Uchida Y., Shibata K., 1985, PASJ, 37, 515
- Vaytet N., Commerçon B., Masson J., González M., Chabrier G., 2018, A&A, 615, A5. doi:10.1051/0004-6361/201732075
- Wurster J., Price D. J., Bate M. R., 2016, MNRAS, 457, 1037. doi:10.1093/mnras/stw013
- Wurster J., Bate M. R., Price D. J., 2018, MNRAS, 475, 1859. doi:10.1093/mnras/stx3339
- Wurster J., Bate M. R., Bonnell I. A., 2021, MNRAS.tmp. doi:10.1093/mnras/stab2296
- Xu W., Kunz M. W., 2021, MNRAS, 502, 4911. doi:10.1093/mnras/stab314
- Wu Y., Wei Y., Zhao M., Shi Y., Yu W., Qin S., Huang M., 2004, A&A, 426, 503. doi:10.1051/0004-6361:20035767

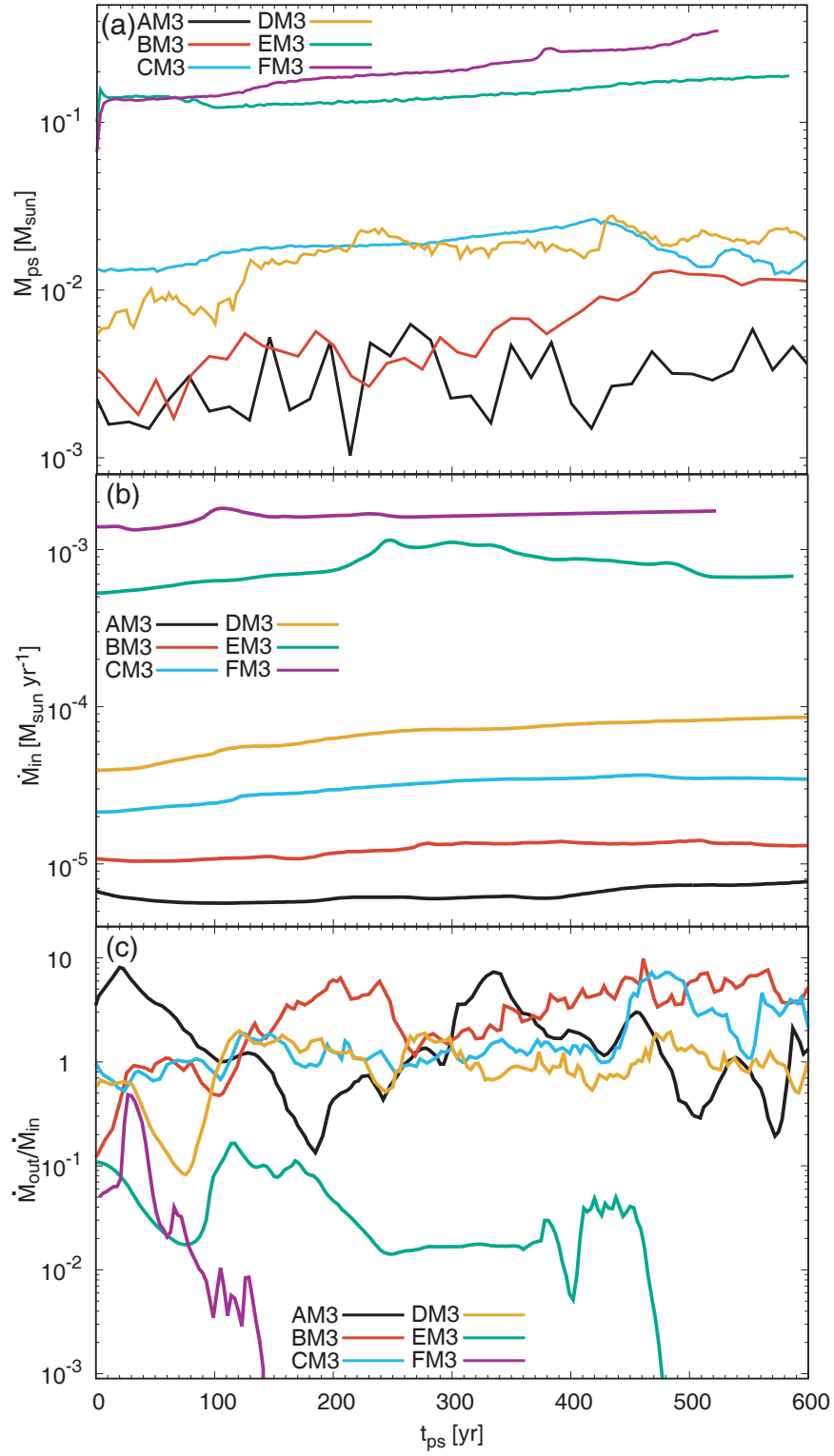


Figure 10. Protostellar mass (a), inflow rate (b) and ratio of outflow to inflow rate (c) against the elapsed time after protostar formation for AM3–FM3.

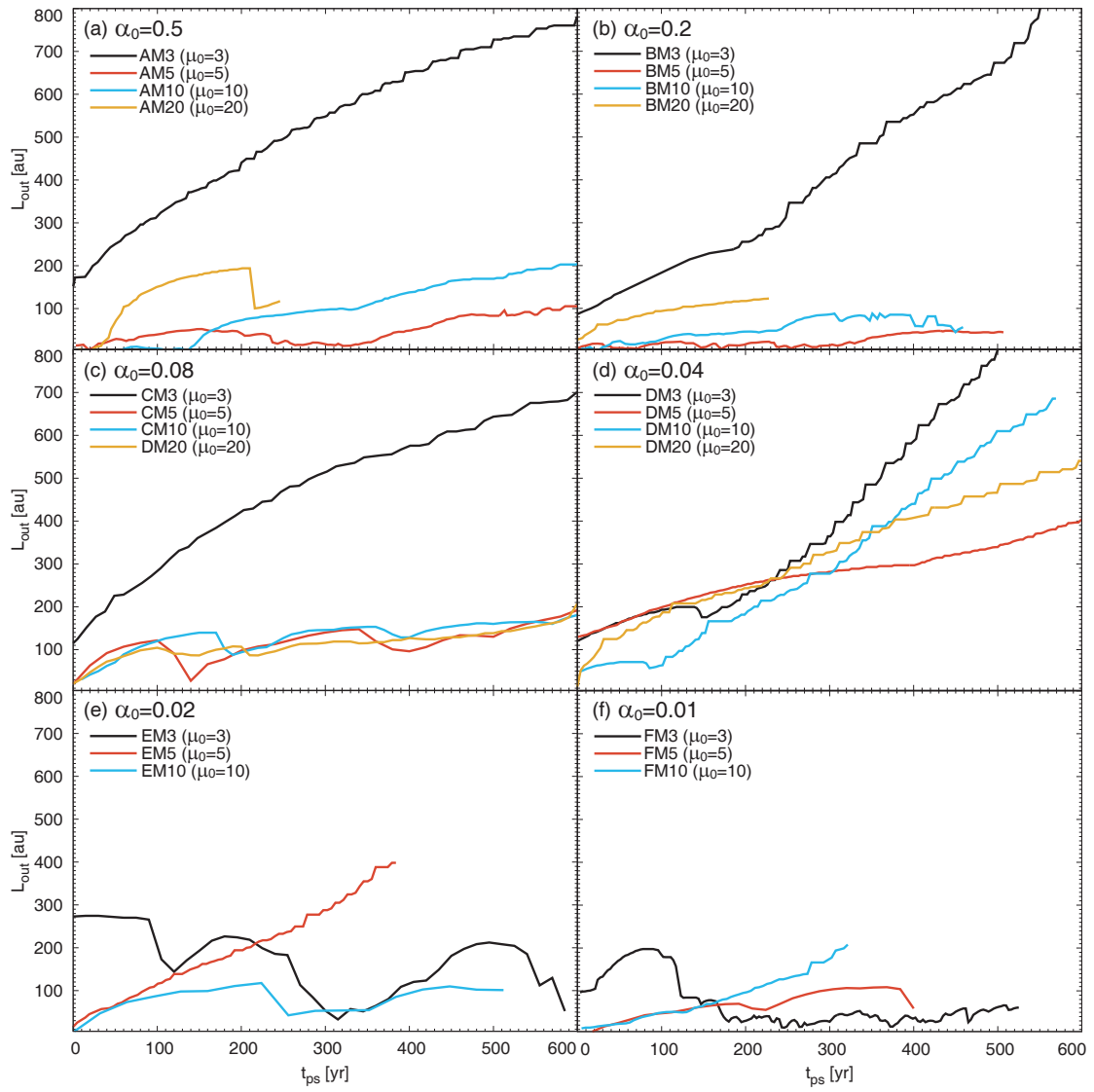


Figure 11. Outflow length against the elapsed time after protostar formation for all models. The model name and parameters α_0 and μ_0 are described in each panel.

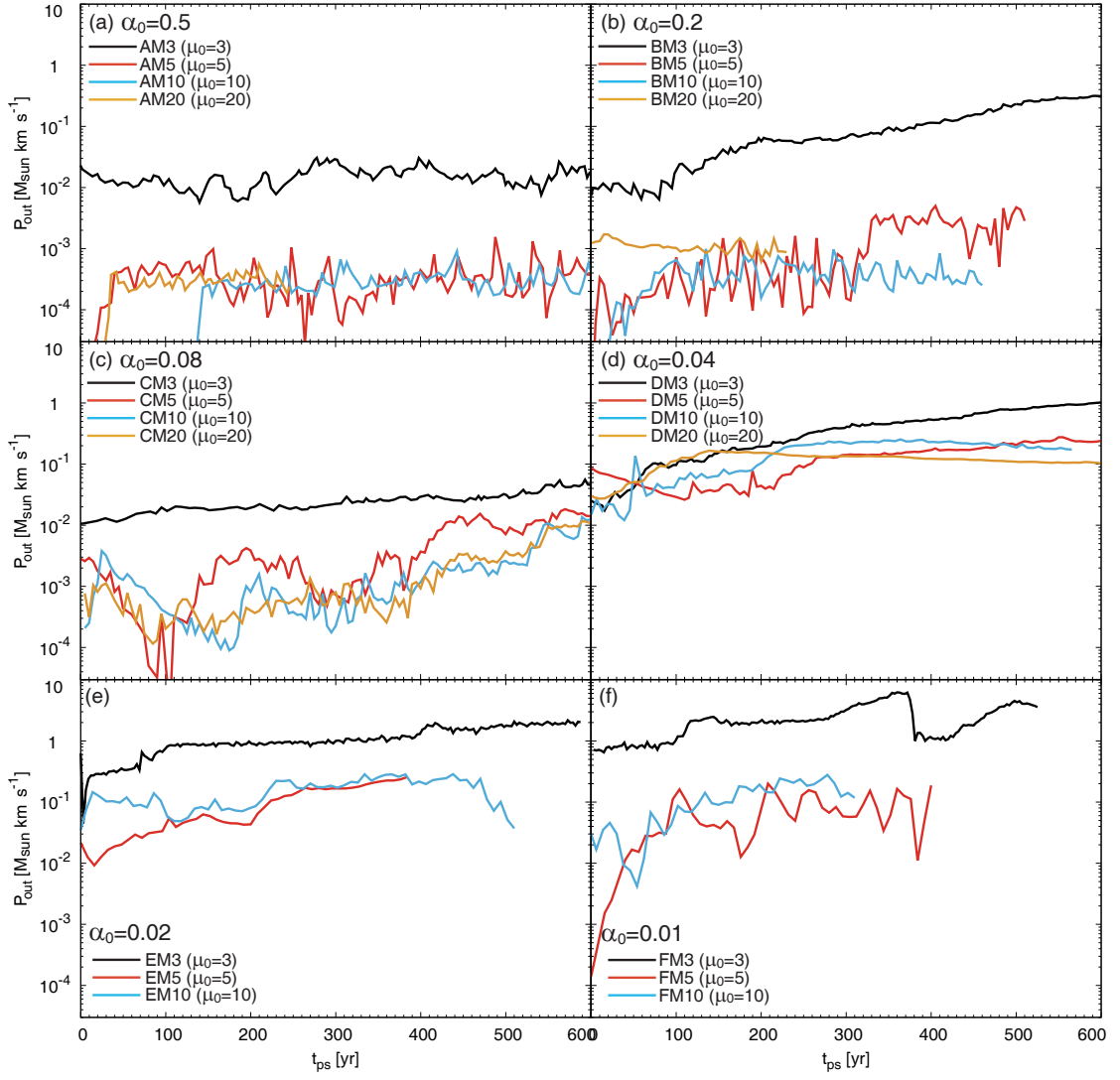


Figure 12. Outflow momentum for all models against the elapsed time after protostar formation. The model name and parameters α_0 and μ_0 are described in each panel.

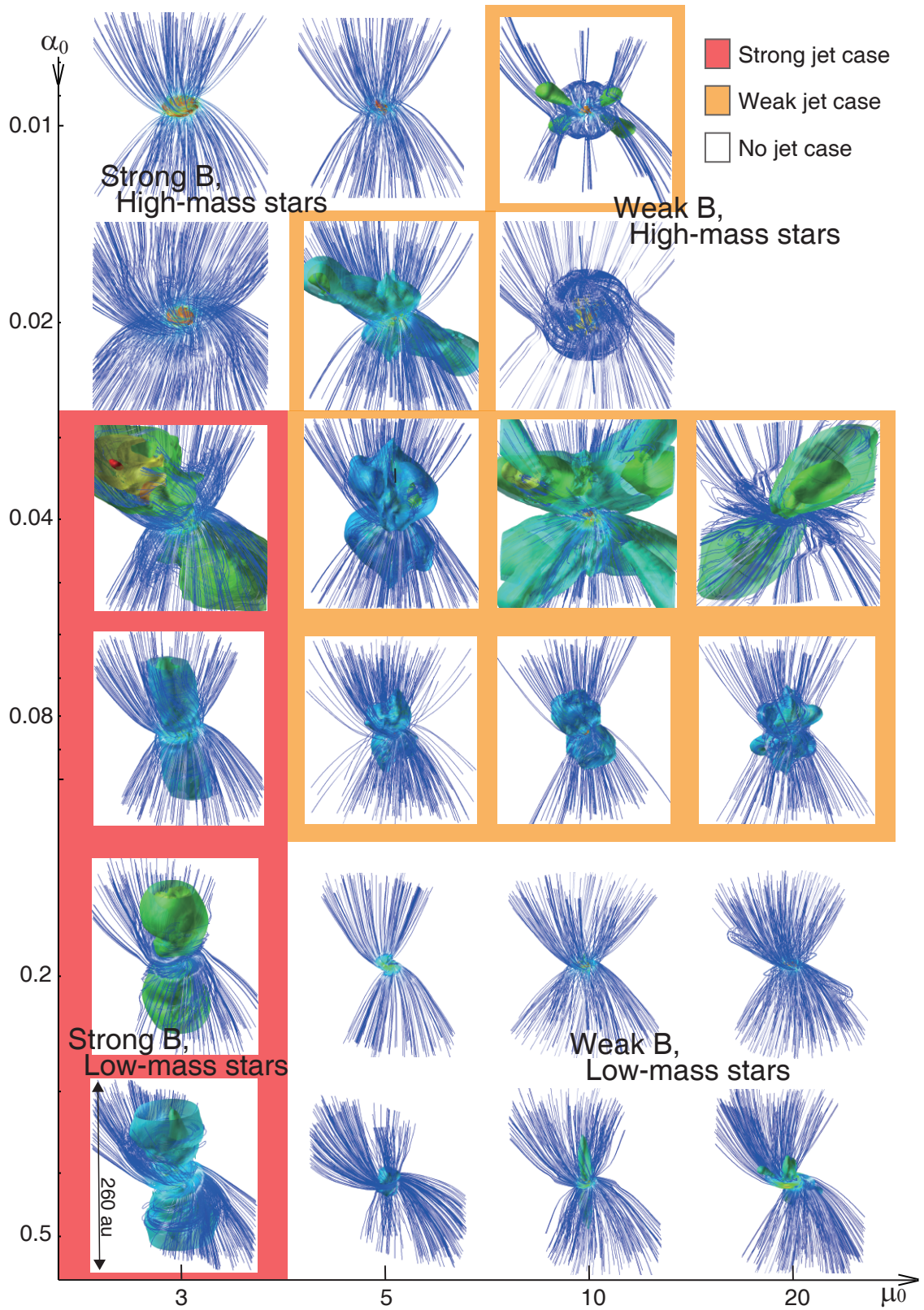


Figure 13. Three dimensional structure at the end of the simulation plotted on the parameter plane (μ_0 and α_0). In each panel, the magnetic field lines (blue stream lines), outflowing component (green, yellow and red iso-velocity surfaces) and disk-like structure (orange iso-density surface) are plotted. Strong (red), weak (orange) and no (white) jet models are represented by the background color.

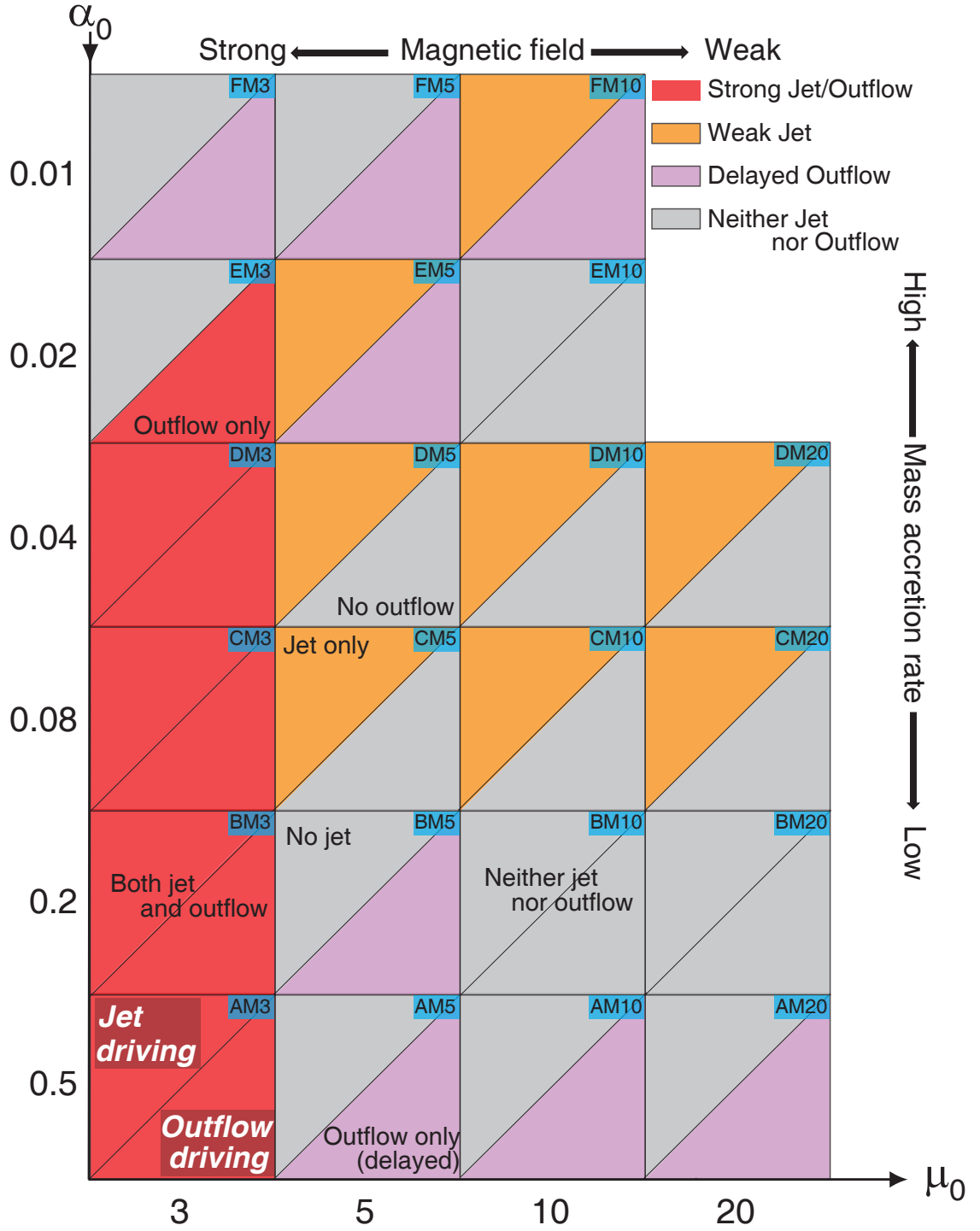


Figure 14. Outcomes of this study and Paper III plotted on the parameter plane (μ_0 and α_0). The model name is described in each panel. In each panel, the outcomes of this study (i.e. jet driving) and that of Paper III are represented by color in the upper left and the lower right, respectively. Color is used to indicate strong jets (upper left) or strong outflow (lower right) (red), no jet (this study, upper left) or no outflow (Paper III, lower right) (gray), a weak jet having a low momentum in this study (orange) and an outflow in a delayed fashion in Paper III (purple).